(2)

NAVAL POSTGRADUATE SCHOOL
Monterey, California

THESIS

AIRCRAFT OBSERVATIONS OF THE ATMOSPHERIC BOUNDARY LAYER IN THE VICINITY OF THE MARGINAL ICE ZONE UNDER CONDITIONS OF FLOW PARALLEL TO THE ICE EDGE

by

Teresa M. Gobel

September 1990

Thesis Advisor W.J. Shaw

REPORT DOCUMENTATION PAGE

1a Report Security Classification Unclassified			1b Restrictive Markings
2a Security Classification Authority			3 Distribution/Availability of Report Approved for public release; distribution is unlimited.
2b Declassification-Downgrading Schedule			
4 Performing Organization Report Number(s)			5 Monitoring Organization Report Number(s)
6a Name of Performing Organization Naval Postgraduate School	6b Office Symbol *(if applicable)* MR		7a Name of Monitoring Organization Naval Postgraduate School
6c Address *(city, state, and ZIP code)* Monterey, CA 93943-5000			7b Address *(city, state, and ZIP code)* Monterey, CA 93943-5000
8a Name of Funding,Sponsoring Organization	8b Office Symbol *(if applicable)*		9 Procurement Instrument Identification Number
8c Address *(city, state, and ZIP code)*			10 Source of Funding Numbers
		Program Element No	Project No / Task No / Work Unit Accession No

11 Title *(include security classification)* AIRCRAFT OBSERVATIONS OF THE ATMOSPHERIC BOUNDARY LAYER IN THE VICINITY OF THE MARGINAL ICE ZONE UNDER CONDITIONS OF FLOW PARALLEL TO THE ICE EDGE

12 Personal Author(s) Teresa M. Gobel

13a Type of Report	13b Time Covered	14 Date of Report *(year, month, day)*	15 Page Count
Master's Thesis	From To	September 1990	55

16 Supplementary Notation The views expressed in this thesis are those of the author and do not reflect the official policy or position of the Department of Defense or the U.S. Government.

17 Cosati Codes			18 Subject Terms *(continue on reverse if necessary and identify by block number)*
Field	Group	Subgroup	Marginal Ice Zone.

19 Abstract *(continue on reverse if necessary and identify by block number)*

This paper describes aircraft observations made with the NOAA P-3 research aircraft on 24 March 1989. The measurement region was over the marginal ice zone, southeast of Spitzbergen, between 74 to 76° N and 19 to 27° E. Above the atmospheric boundary layer, the geostrophic wind was 12 m s^{-1} at approximately 15° off-ice. A well mixed layer extended along the entire 200 km flight path which was perpendicular to and centered over the ice edge. There was a stratocumulus layer over the ocean which decreased in thickness towards the ice. The associated inversion, which coincided with the cloud layer top, continued to decrease in height over the ice. This caused a strong thermal wind effect within the atmospheric boundary layer. The near-surface geostrophic wind decreased from approximately 12 m s^{-1} over the ocean to 5 m s^{-1} over the ice due to the horizontal temperature gradient and sloping inversion.

20 Distribution/Availability of Abstract	21 Abstract Security Classification	
☒ unclassified,unlimited ☐ same as report ☐ DTIC users	Unclassified	
22a Name of Responsible Individual W.J. Shaw	22b Telephone *(include Area code)* (509) 376-5575	22c Office Symbol MR/Sr

DD FORM 1473,84 MAR 83 APR edition may be used until exhausted
All other editions are obsolete

Approved for public release; distribution is unlimited.

Aircraft Observations of the Atmospheric Boundary Layer in the Vicinity of the Marginal Ice Zone under Conditions of Flow Parallel to the Ice Edge

by

Teresa M. Gobel
Lieutenant, United States Navy
B.A., Ithaca College, 1975

Submitted in partial fulfillment of the
requirements for the degree of

MASTER OF SCIENCE IN METEOROLOGY AND OCEANOGRAPHY

from the

NAVAL POSTGRADUATE SCHOOL
September 1990

Author: Teresa M. Gobel

Teresa M. Gobel

Approved by:

W.J. Shaw, Thesis Advisor

W.A. Nuss, Second Reader

Robert L. Haney, Chairman,
Department of Meteorology

ABSTRACT

This paper describes aircraft observations made with the NOAA P-3 research aircraft on 24 March 1989. The measurement region was over the marginal ice zone, southeast of Spitzbergen, between 74 to 76° N and 19 to 27° E. Above the atmospheric boundary layer, the geostrophic wind was 12 m s^{-1} at approximately 15° off-ice. A well mixed layer extended along the entire 200 km flight path which was perpendicular to and centered over the ice edge. There was a stratocumulus layer over the ocean which decreased in thickness towards the ice. The associated inversion, which coincided with the cloud layer top, continued to decrease in height over the ice. This caused a strong thermal wind effect within the atmospheric boundary layer. The near-surface geostrophic wind decreased from approximately 12 m s^{-1} over the ocean to 5 m s^{-1} over the ice due to the horizontal temperature gradient and sloping inversion.

TABLE OF CONTENTS

LIST OF TABLES

LIST OF FIGURES

I. INTRODUCTION

A. ARCTIC ICE EDGE METEOROLOGY

Desire to make use of the Arctic polar region resources has greatly increased man's activity there. Understanding the environment is vital in order to tap the immense discoveries of oil, natural gas and rich fisheries. The relationship between global weather and the polar ice cap has also been an item of long standing interest. In the Arctic, between 1953 and 1977, the average maximum extent of the sea ice was 14 million km², which is 5% of the northern hemisphere. The minimum extent was 7 million km² (Walsh and Johnson, 1979). How this annual variation in ice cover is related to large-scale and mesoscale circulations is not fully understood.

The marginal ice zone (MIZ) is the transition region between the open ocean where there is no sea ice and the polar ice pack with 80% or greater ice cover. Large horizontal gradients in ice, ocean and atmospheric properties characterize the region. Also, strong interactions between the ice, ocean and atmosphere occur. The spatial variation of the atmospheric boundary layer (ABL) thermal structure and surface roughness differences between the ice and ocean cause secondary atmospheric and oceanic circulations near the ice edge.

Warm ocean currents limit the extent of the ice cover. The wind controls the concentration of ice in the MIZ (Davidson and Guest, 1987). The ice characteristics from the polar ice cap across the MIZ vary. Overland et al. (1983) describe the MIZ by three ice regions: 1) a smooth, interior ice pack region of large ice floes with 1 km horizontal and 2 to 3 m vertical dimension; 2) a transition zone of small rectangular floes with 20 m horizontal and 3 to 6 m vertical dimension; and 3) a rough zone of small, broken floes with less ice concentration than zone two. These varying conditions of surface roughness affect the wind and interactions between the atmosphere, ice and ocean.

The ice is relatively fresher than the ocean. The melting and freezing of the ice can affect the temperature, salinity, and vertical density structure of the upper ocean. The change in surface stress across the MIZ is believed to cause ocean upwelling near the ice edge (McPhee, 1983).

The atmosphere's temperature markedly varies across relatively short distances, from warmer temperatures over the ocean to very cold over the ice. Atmospheric stability can also experience abrupt variation. Over the ocean, the atmosphere is typically

unstable, while over the ice it is stable to slightly unstable. Strong inversions are common. Shapiro and Fedor (1989) observed very intense cyclones, referred to as polar lows, which formed as an arctic cold-air outbreak and cold front moved from the MIZ out over the warmer ocean.

Observations in the MIZ are limited by the region's remoteness and the resulting logistic difficulties that this imposes. Various multidisciplinary experiments have made observations of interactions between the ice, ocean and atmosphere. The Arctic Ice Dynamics Joint Experiment (AIDJEX) was a five year project in the 1970s to determine ice pack motion and its causes. Using AIDJEX data, Thorndike and Colony (1982) studied the causes of average ice motion. They found the long-term average wind and the upper-level circulation of the ocean equally contribute to the long-term (several months) average ice motion for distances greater than 400 km from a land boundary. The ice motion fluctuations (after removing the mean motion) are more closely related to the geostrophic wind than to the ocean current. The geostrophic wind accounted for 70% of the variance of the ice velocity. Within 400 km of land, the effect of the coastline on internal ice stresses also contributes to the ice motion. From the Norwegian Remote Sensing Experiment in 1979, Johannessen et al. (1983) found a correlation between wind direction and ice edge convergence/divergence. With on-ice flow the MIZ is more compact than with off-ice flow.

The most extensive documented ABL observations in the MIZ have come from the Marginal Ice Zone Experiment (MIZEX) in the Bering and Greenland Seas during 1983 and 1984. Johannessen (1987) describes the summer MIZEX East program in Fram Strait and the Greenland Sea. Fairall and Markson (1987) show the variation of surface fluxes for five aircraft flights during July 1983 over the MIZ in the Greenland Sea. Conditions for the five flights include winds from all four directions relative to the ice edge at wind speeds 7 m s^{-1} and below. They noted that the wind direction and its effect on atmospheric stability, can be an important factor in describing the surface stress. On-ice flow or flow parallel to the ice edge from the south at less than 5 m s^{-1}, caused more stable conditions in the MIZ. Under these conditions, the effects of hydrostatic stability on surface stress were the same order of magnitude as the effect due to varying surface roughness. Kellner et al. (1987) document turbulence statistics and spectra under conditions of off-ice flow in the Fram Strait. This study includes aircraft and shipboard observations made during the summer of 1984. The mixed layer depth increased towards the ocean as convective mixing from the warmer ocean became important. This coincided with a shift in the peak frequency of the vertical wind component's

variance spectra from 1 Hz (100 m) over the ice to .4 Hz (250 m) over the ocean. Secondary low frequency peaks were evident over the ocean. These indicated secondary circulations.

Early numerical models of the MIZ simulated off-ice flow. Overland et al. (1983) used a one-layer slab model to show the evolution of the ABL. The wind velocity in the ABL and the height of the base of the inversion proved sensitive to the surface roughness decrease and heat flux increase from ice to ocean. By 50 km oceanward of the ice edge, the horizontal temperature gradient had caused an 8% increase in wind speed. Roughness changes were responsible for a 9% wind speed increase across the MIZ (approximately 35 km). The base of the inversion slowly increased towards the ocean. This study agreed with the observation that an off-ice wind field contributes to ice edge divergence. Reynolds (1984) enhanced the slab model by including cloud and radiation effects. The addition of cloud and radiation effects for off-ice flow, slightly increased the slope of the inversion base and slightly decreased the wind speed. Such a slab model adequately simulates the shallow boundary layer of off-ice flow, but for flow from other directions, a more sophisticated model is needed.

Bennett and Hunkins (1986) used a multilevel, two-dimensional, higher-order closure model to simulate on-ice flow. The model included stratus cloud effects and sea ice thermodynamics. They used observed data to set the model's initial conditions of wind and potential temperature profiles at the ice edge. The processes of turbulence, lateral and vertical advection and radiation were simulated. The model showed good agreement with the observed vertical soundings at various distances from the ice edge. The base of the inversion increased from 500 m at the ice edge to 1000 m at 150 km iceward of the ice edge. The study confirmed the importance of including cloud top longwave cooling when modeling a cloud topped ABL under conditions of on-ice flow. The model results suggested that the boundary layer cooling away from the ice edge was mainly due to cloud top longwave cooling, not downward heat flux.

Kantha and Mellor (1989) used a two-dimensional, higher-order closure model to simulate off-ice, on-ice, and along-ice flow. For off-ice flow, the model showed good agreement with the Overland et al. (1983) results. With on-ice flow where there was strong heat flux from the ABL to the ice, an inversion tens of meters in depth and a strong jet resulted. For along-ice flow with a slight component either on or off-ice, a strong thermal ice edge front with intense turbulence resulted. The number of detailed descriptions of the ABL over the MIZ from observations are few. More observations are needed to validate the model results.

B. CEAREX

The Eastern Arctic Aircraft Expedition, which took place in March 1989, was a component of the multinational, interdisciplinary Coordinated Eastern Arctic Experiment (CEAREX). This expedition provided the opportunity to investigate the structure of the ABL in the vicinity of the MIZ in the Barents Sea using the NOAA P-3 research aircraft.

Under conditions of flow nearly parallel to the ice edge, one flight was made on 24 March 1989 to make measurements of the ABL, the background atmospheric structure, and turbulent fluxes using a gust-probe. This paper discusses the observations of that flight. This is the first set of observations to provide a comprehensive description of ABL structure over the MIZ for flow nearly parallel to the ice edge.

II. THE DATA

A. FLIGHT DESCRIPTION AND CONDITIONS

The U.S. Navy Fleet Numerical Oceanography Center's surface pressure analysis of 1200 Coordinated Universal Time (UTC), 24 March 1989 (Figure 1) depicted two low pressure centers, one west of Norway at 60° N and 0° E and one at approximately 73° N and 50° E. There was a short inverted ridge where the isobars and wind trajectories curve south between these two low pressure centers. In the vicinity of the short inverted ridge, which included the measurement area centered at approximately 75° N and 23° E, the wind direction varied. The flow in the measurement area was northeasterly. To the east of the measurement area the flow was more northerly, while to the west it was easterly.

During the aircraft's approach to the measurement area, stratocumulus clouds were observed over the open ocean with some precipitation beneath the clouds. This cloud layer thinned towards the ice edge and there were no clouds over the ice.

The criterion for the flight was that the wind flow would be nearly parallel to the ice edge, with a small off-ice component so boundary layer operations would not be limited by fog. With the criterion met, measurements were made in the MIZ southeast of Spitzbergen on 24 March 1989 between 74 to 76° N and 19 to 27° E. The MIZ itself was fairly compact. The ice pack (with greater than 80% ocean cover) followed a 10 to 20 km zone of pancake ice. The ice edge was oriented northeast-southwest as indicated by the dashed line in Figure 2.

The aircraft speed during measurements was approximately 100 m s^{-1}. The flight pattern (Figure 3) included:

- Four 200 km legs perpendicular to the ice edge at 900, 800, 700 mb and 45 m which were almost exactly centered over the MIZ.

- Two legs approximately 50 km in length over the ice at 33 and 150 m, parallel to the ice edge.

- Two legs approximately 50 km in length over the ice at 75 and 150 m, perpendicular to the ice edge.

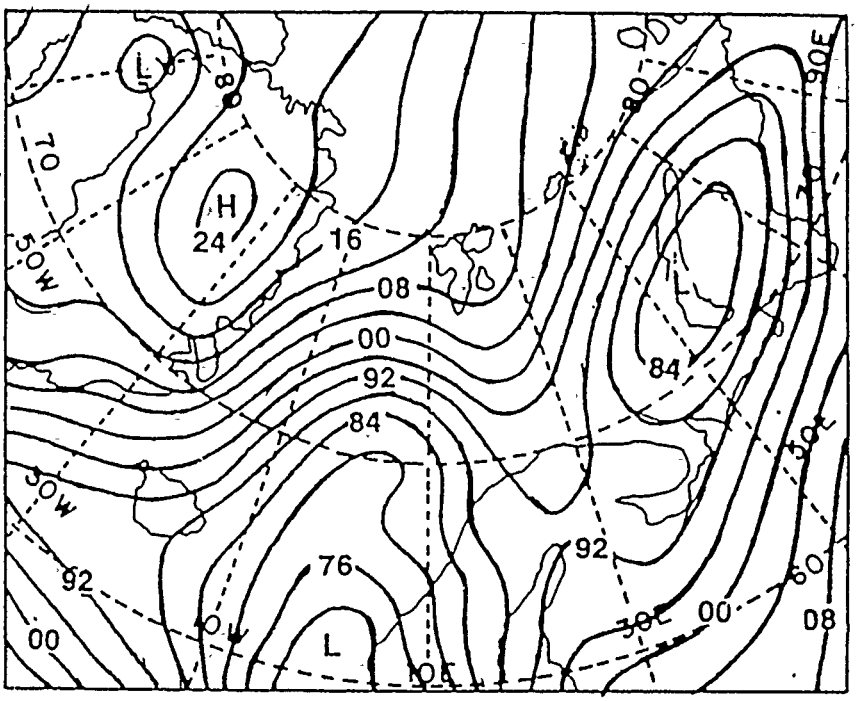

Figure 1. Surface pressure analysis
Source: Lackmann et al., (1989)

- Two legs approximately 50 km in length over the ocean at 45 and 267 m, parallel to the ice edge.

- Two legs approximately 50 km in length over the ocean at 135 and 267 m, perpendicular to the ice edge.

B. INSTRUMENTATION

The ABL mean and turbulent variables were measured from the NOAA P-3. Obtaining a wind measurement with respect to the earth requires determining both the aircraft's velocity with respect to the earth and the velocity of the air with respect to the aircraft. An inertial navigation system (INS) provided the aircraft velocity and position with respect to the earth. The mean velocity of the air with respect to the aircraft was obtained using a pitot-static tube. A forward port on the tube gives a total pressure

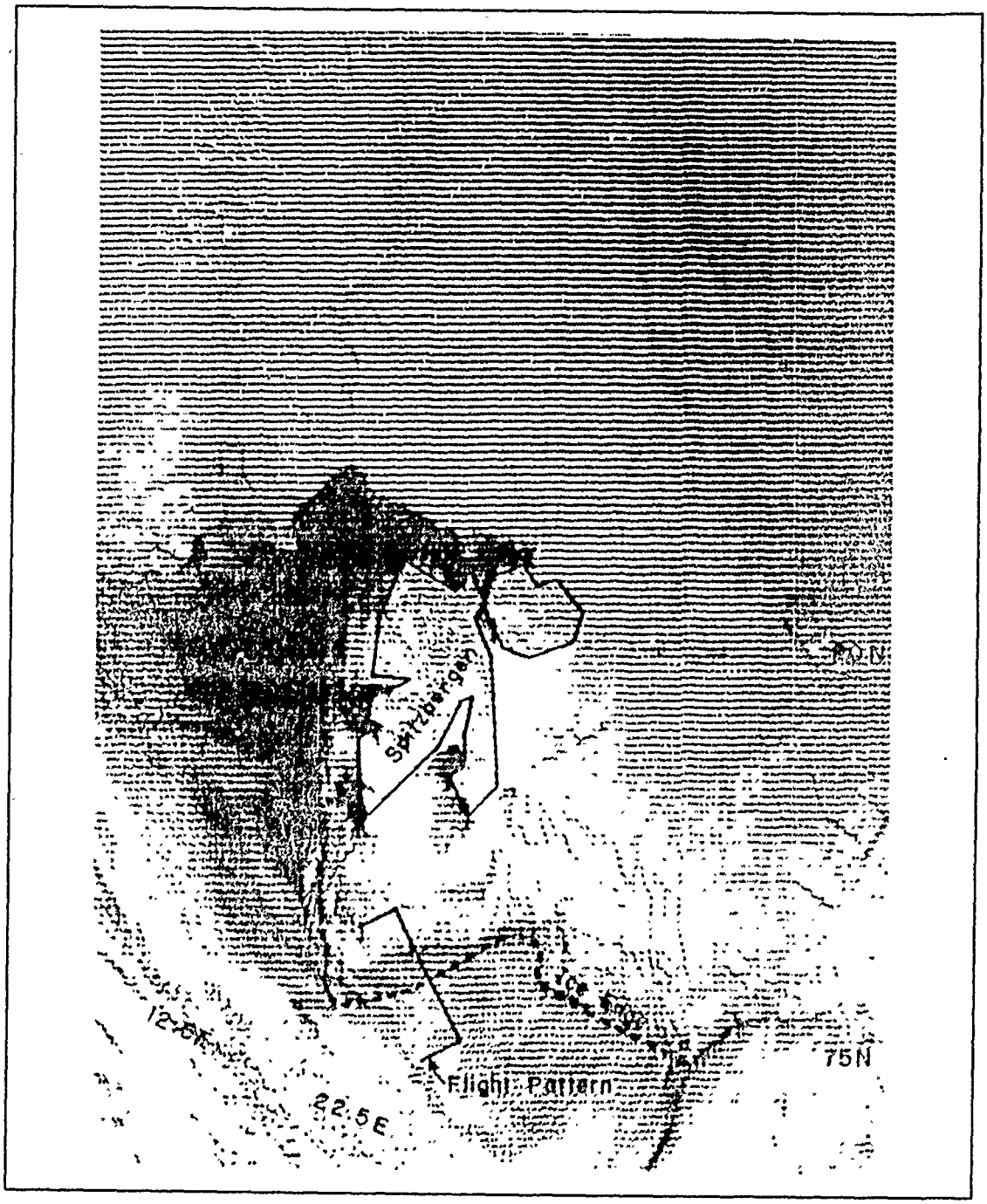

Figure 2. NOAA-10 IR imagery of 1038 UTC 24 March 1989

measurement and side ports give static pressure. The difference between these two pressures is a measure of dynamic pressure. Combining this dynamic pressure meas-

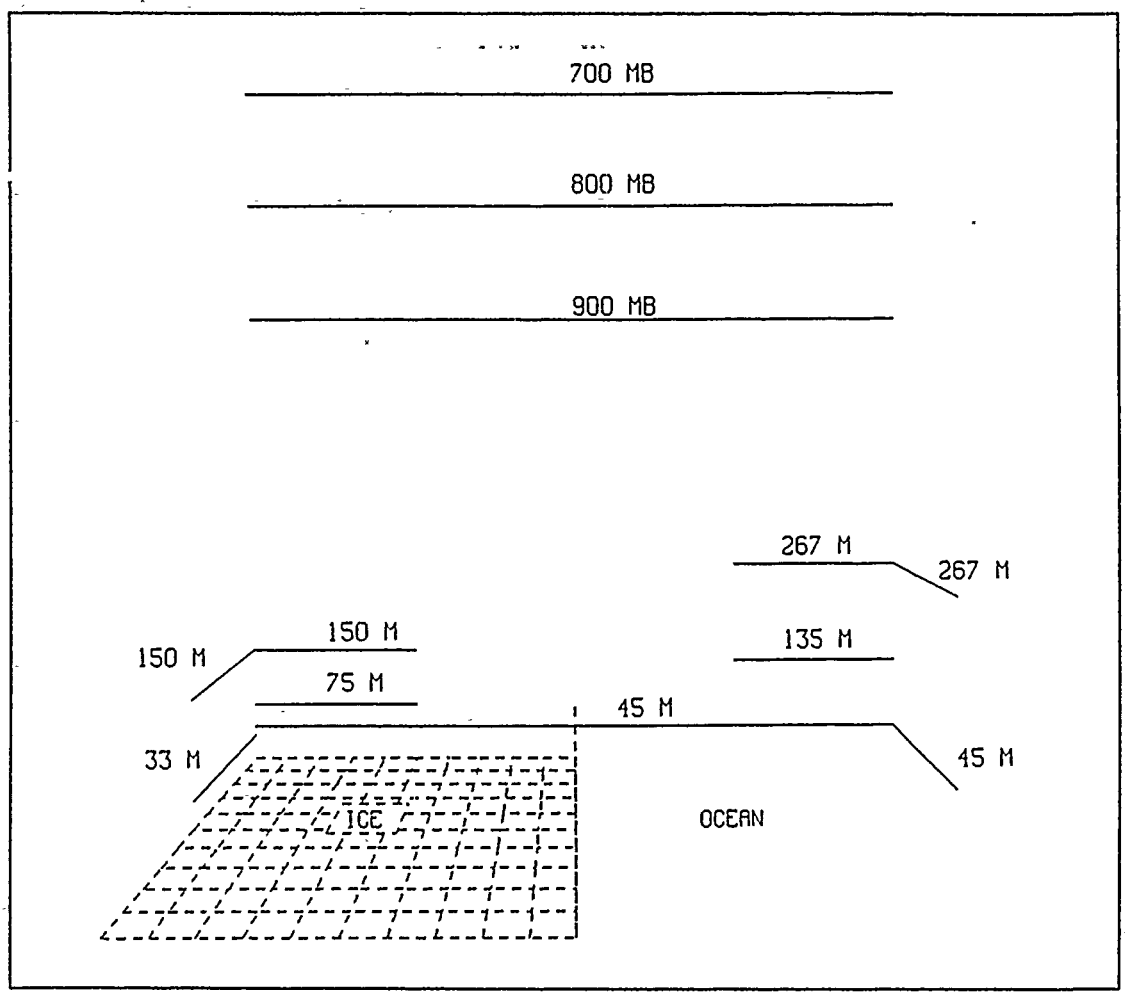

Figure 3. Flight pattern schematic for CEAREX flight

urement with ambient temperature and static pressure measurements gives the mean wind speed. The wind direction was obtained from vanes attached to the tube. The turbulent wind measurements were obtained using a gust probe whose performance is described by Greenhut and Gilmer (1985).

A Rosemount total temperature probe was used to obtain the mean temperature. Total temperature refers to the ambient temperature plus dynamic heating (the effect of air flow on the sensor). A .025 mm platinum wire sensing element experiences changes in specific resistance which are proportional to the change in temperature. This

same principal is used by the bead thermistor which gave the temperature measurement as part of the turbulence package. The sea surface temperature was remotely sensed by a Barnes PRT-5 radiometer. It compared the radiance of the sea surface in the 9.5 to 11.5 μm wavelength band with that of an internal reference cavity.

A dewpoint hygrometer provided an absolute measure of humidity (mass per unit volume). A mirror is maintained at the temperature where the moisture in the air just begins to condense on it. The condensation is monitored optically. This sensor was slow to respond to a change in the measured variable compared to the other sensors. It took tens of seconds to reach equilibrium. Another part of the gust probe system, a microwave refractometer, measured the turbulent moisture fluctuations. This sensor directly measures fluctuations in the radio refractive index. Combining this measurement with those of temperature and static pressure gives the water vapor density.

There was also a lidar system on board the NOAA P-3 which was operated by University of Washington personnel. The system transmitted two laser light beams every second, of wavelengths .532 and 1.046 μm. The transmitted light is strongly scattered by cloud droplets. A telescope collects the returned light and focuses it on a detector. From there it is amplified, digitized every 20 ns and recorded. This resulted in a resolution of 7.5 m. Cloud base and cloud top height measurements were obtained using the lidar. Table 1 lists the variables, their sampling rates and the sensors used.

Table 1. INSTRUMENTATION CARRIED BY THE NOAA P-3 IN CEAREX.

Mean Variables	Sampling Rate (s^{-1})	Instrument Source
u, v	1	Pitot-static system combined with INS
T	1	Rosemount Total Temperature Probe 102CH2AF
Dewpoint	1	General Eastern 120DEP Dewpoint Hygrometer
Altitude	1	Radar altimeter (Stewart-Warner APN159)
Pressure	1	Rosemount 542K2
Sea surface temperature	1	Barnes PRT-5 Radiometer
Turbulent Variables	**Sampling Rate (s^{-1})**	**Instrument Source**
u, v, w	40	Gust probe combined with INS
T	40	Bead thermistor
q	40	Microwave refractometer

C. DATA PROCESSING

Most of the mean variable sensors were checked by comparing their measurements against routine observations taken at Bodo, Norway, where the CEAREX flights originated. This comparison revealed:

- The dewpoint hygrometer observations were 5.6° too cold.
- Temperature data were within 1° K and pressure data within 1 mb.

The radiometer used to obtain the surface temperature was calibrated at NOAA's Office of Aircraft Operations (OAO) in Miami, prior to and after the CEAREX flights. These checks showed a drift of 2° K at -35° C and 1° K near freezing.

Inertial navigation systems (INS) generally experience slowly varying drifts with time. It was planned to use the Loran-C navigational aid signal to compensate for this following the flight. However, the Loran-C signal was too weak to use. So, the possibility exists that INS drift could have introduced variations as large as 3 m s^{-1} in the wind field (Shaw, 1988).

Greenhut and Gilmer (1985) described the calibration and performance of the gust probe system. The thermistor is calibrated in a wind tunnel to correct for dynamic heating. This correction is approximately 4° C at an air speed of 100 m s^{-1}. The characteristics of the microwave refractometer are also well known. The gust probe system performance during a set of aircraft maneuvers (called the Lenschow maneuvers) is well established. During the CEAREX flight, these Lenschow maneuvers were executed. Later evaluation of the gust probe system data during these maneuvers identified any abnormalities in the performance of the system.

The gust probe system was mounted on a boom attached to the nose of the aircraft. The boom length was chosen so its natural frequency is about 14 Hz. Frequencies greater than 11.5 Hz are filtered out of all the gust probe system signals on-board the aircraft, prior to recording the data. This avoids aliasing the higher frequency natural resonances of the boom and other sensors into the recorded data.

Two separate data streams of mean and turbulent (gust probe) observations were recorded, with UTC being the only common variable. The mean data were initially processed at NOAA's Office of Aircraft Operations (OAO) in Miami. All the above noted errors were corrected and the data were screened for unrealistic values.

The turbulence data were initially processed at NOAA's Environmental Research Laboratories (ERL) in Boulder, Colorado. The turbulent fluxes were determined using the eddy correlation method at the Naval Postgraduate School. It was desired to show the variation of the boundary layer fluxes compared to the surface variability and also,

to use Fast Fourier Transforms (FFT) which use less computer time than other methods. To accomplish this, the data (time series) were analyzed in 102.4 s segments corresponding to about 10 km of sampling distance. This 102.4 s segment length met the FFT requirement of 2^n data points per segment. The sampling rate was 40 s^{-1}, yielding 4096 (2^{12}) points per Fourier transform.

As noted earlier, the recorded gust probe system data included frequencies up to 11.5 Hz. The first step was to pass the time series through a high-pass symmetric compound running mean subtraction filter (Holland, 1968). This eliminated the unwanted low frequency (mean) information from the time series, leaving the high frequency (perturbation or turbulent) part. The filter parameters were set such that more than 90% of signal variance was removed for wavelengths longer than 10 km (Shaw et al., 1990). This is equivalent to the filter eliminating 90% of the signal information for frequencies less than .01 Hz. This particular filter was chosen for its efficiency and ease of implementation. Another benefit of using this particular filter was that its transfer function is well-behaved and does not seriously distort the other frequencies in the time series. The filter passed a small amount of signal variance for frequencies of .01 to .03 Hz, and all signal variance for frequencies greater than .03 Hz. It was desired to retain signal information for frequencies of .01 Hz and greater. The information that was eliminated for frequencies .01 to .03 Hz was reinserted during a later step.

Next, Fast Fourier Transforms (FFT) were performed on each 102.4 s segment and the spectra and cospectra were calculated. The one-sided spectra and cospectra, $G_{aa}(f)$ and $G_{ab}(f)$ where a and b are are any two variables and f is frequency, describe the variance and covariance distributed over frequency. The variance and covariance are defined:

$$\overline{a'^2} = \int_0^\infty G_{aa}(f)df$$

$$\overline{a'b'} = \int_0^\infty G_{ab}(f)df$$

The covariances represent turbulent fluxes (Sorbjan 1989). For example, the vertical temperature flux (w'T') is a covariance between the turbulent or perturbation quantities (denoted by the prime) of vertical motion (w') and temperature (T').

The third step was to divide the spectra and cospectra by the transfer function of the compound running mean subtraction filter, which was applied in the time domain. The transfer function describes the relation between the signal input to the filter and the filter's output. It is obtained by performing a Fourier Transform on the function describing the filter. The covariance transfer function is a ratio between the covariance after filtering and the covariance before filtering. The cospectra computed in step two is a ratio between covariance after filtering and frequency. Thus dividing the cospectra from step two by the transfer function gives the true cospectra (cospectra before filtering). This relation is also valid for the spectra if variance is substituted for covariance. This step reinserts the .01 to .03 Hz information that was removed by the filtering in step one.

The last step was to integrate the true spectra and cospectra with respect to frequency. This gave the desired average variances and covariances (turbulent fluxes) for each 102.4 s segment.

III. MEAN STRUCTURE

A. VERTICAL STRUCTURE

Vertical profiles were obtained from 10 s averages during altitude changes between the straight and level measurement legs. These altitude changes took place at approximately 100 km from the ice edge over the ice and ocean. The composite virtual potential temperature profile (Figure 4) showed that the ABL was well-mixed at approximately 252° K to about 150 m over the ice and at approximately 263° K to about 750 m over the ocean. Above the ABL, the profiles over both the ice and ocean display nearly identical thermal structure (± 2° K). The composite specific humidity (q) profile (Figure 4) had this same general structure except that over the ocean, the humidity profile was not so well-mixed in the boundary layer.

Four altitude changes were made over the ice. The resulting profiles individually revealed:

- Three of the four virtual potential temperature profiles were well-mixed to about 100 m (Figure 5). There was a slightly stable layer between 100 and 200 m, and a strong capping inversion above 200 m. The fourth profile which was the farthest from the ice edge differed in that the well-mixed layer was approximately 70 m deep and inversion layer was .5° K warmer than the other three profiles. This suggests the inversion was sloping downward sharply toward the ice.

- The dewpoint hygrometer had a tendency to overshoot a step change. Two of the four available specific humidity (q) profiles (Figure 6) were obtained from altitude changes that started within the ABL. These showed a constant q value, characteristic of a well-mixed layer, to a height of 150 m. The other two profiles, one of which was the profile farthest from the ice edge, were obtained from altitude changes that started above the ABL. These showed q variation within the ABL, making identification of the well-mixed layer top less clear. However, for the profile farthest from the ice edge, q began to decrease with height at approximately 70 m. This agrees with the virtual potential temperature finding that the ABL depth for the profile farthest from the ice edge is about one-half that found in the other profiles.

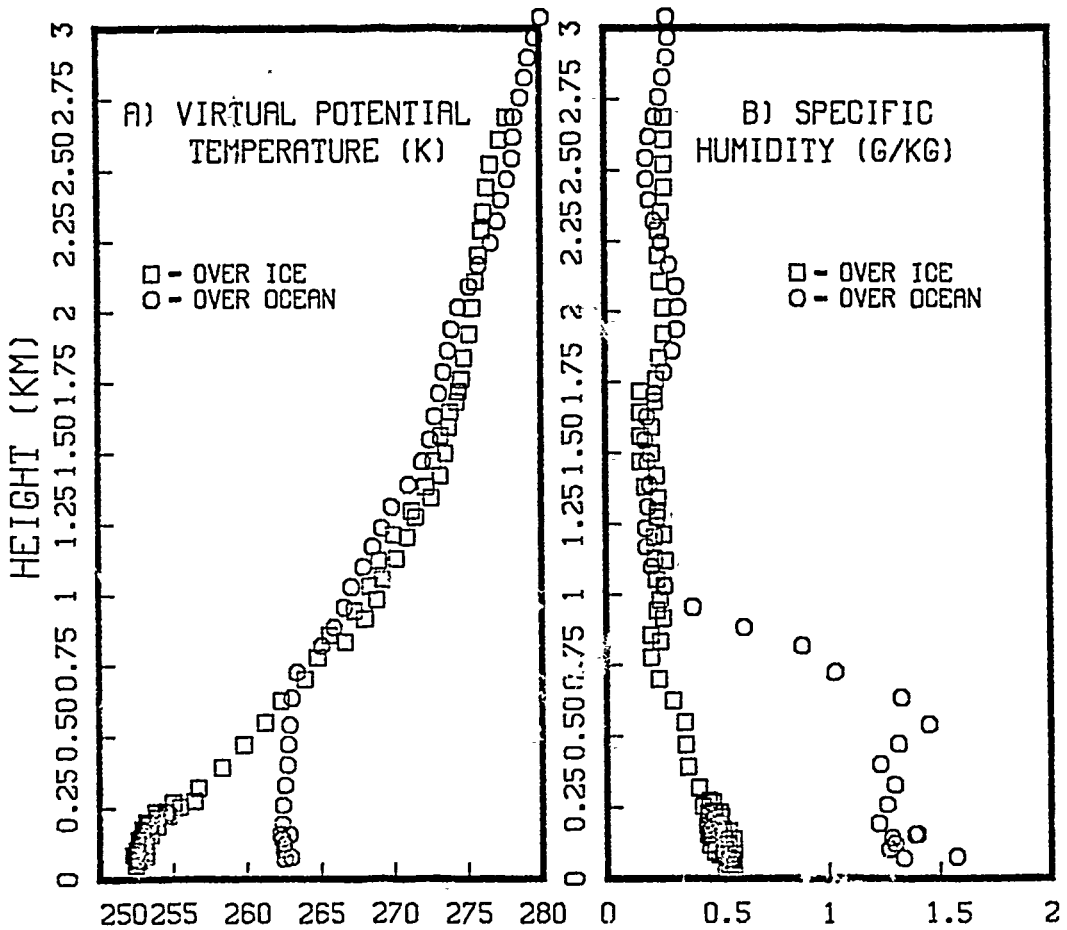

Figure 4. Composite profiles of a) virtual potential temperature and b) specific humidity

- The downstream profiles of virtual potential temperature and specific humidity reflected moistening of the boundary layer and warming due to surface heat flux.

- The wind speed profiles were seriously contaminated by turns and rapid altitude changes. Using only 10 s data segments where the aircraft heading changed less then .5°s^{-1} and the altitude changed less 3 m s^{-1} , the profiles (Figure 7) showed that the ABL wind adjustment to geostrophic value occured almost entirely in the inversion. Between 150 and 250 m, the wind increased by 8 m s^{-1} .

B. CROSS-SECTIONS

Shaw et al., (1990) described the structure of the ABL during the flight. The data from the 200 km flight legs provided cross-sections perpendicular to the ice edge. The

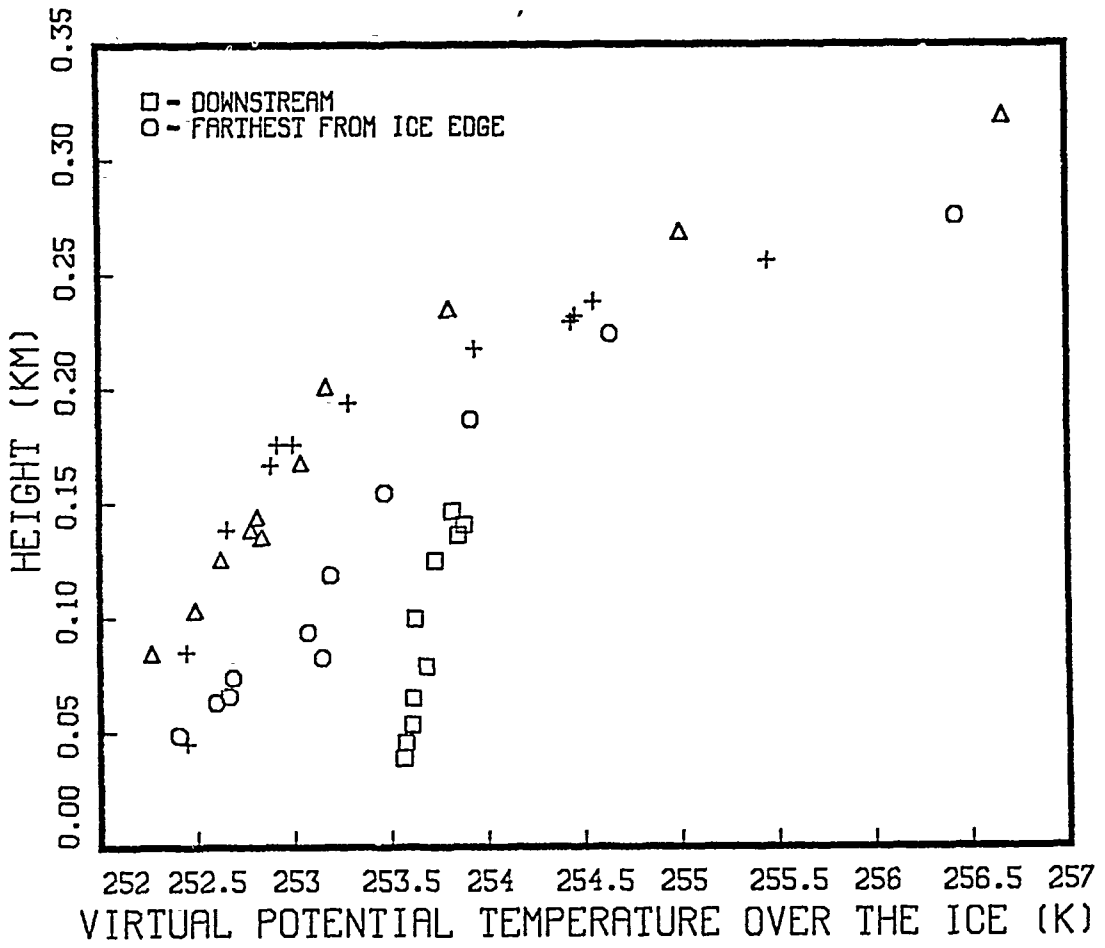

Figure 5. Profiles of virtual potential temperature over ice

radiometric surface temperature cross-section (Figure 8) had a step-like structure. Over the ocean, the surface temperature was slightly above 0° C at distances greater than 40 km from the ice edge and just below 0° C within 40 km of the ice edge. The ice edge was clearly identified by a marked decline in surface temperature, with leads indicated by warm temperature spikes. Twenty kilometers iceward of the ice edge, the radiometric surface temperature had dropped to -15° C and by 60 km to near -25° C.

Virtual potential temperature traces (Figure 8) of the 900, 800, and 700 mb legs reflected near horizontal temperature contours which indicate there was virtually no

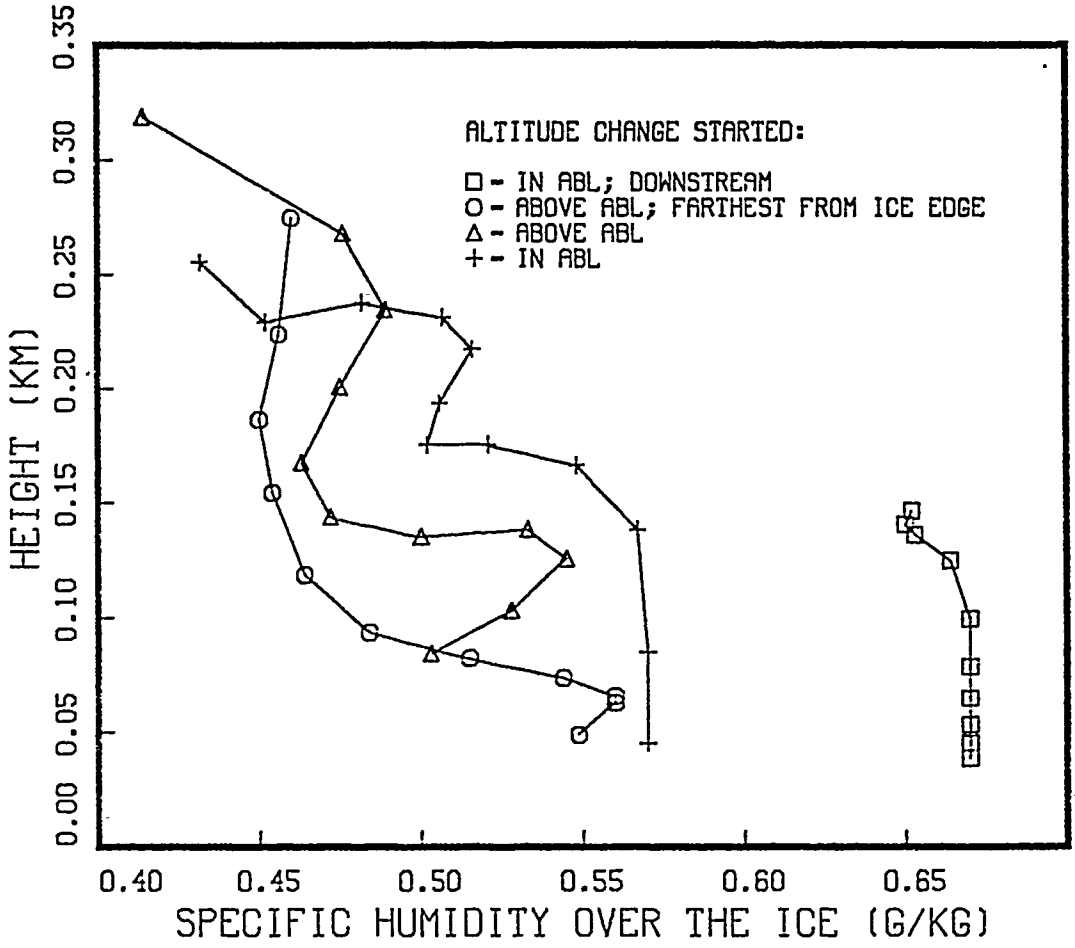

Figure 6. Profiles of specific humidity over ice

change of temperature perpendicular to the ice edge at any altitude above the ABL. Therefore, interactions with the surface are responsible for all cross-ice-edge thermal variability within the ABL. Ocean-ice temperature differences cause baroclinity within the ABL. Consistent with the small off-ice component to the flow, the baroclinity was strongest in the region 40 km oceanward of the ice edge.

Using the lidar pointing downward on the 700 mb leg and upward on the 45 m leg, it was possible to determine the top and bottom of the stratocumulus layer. The stratocumulus layer (shaded region on Figure 8) was 300 to 400 m thick at 100 km

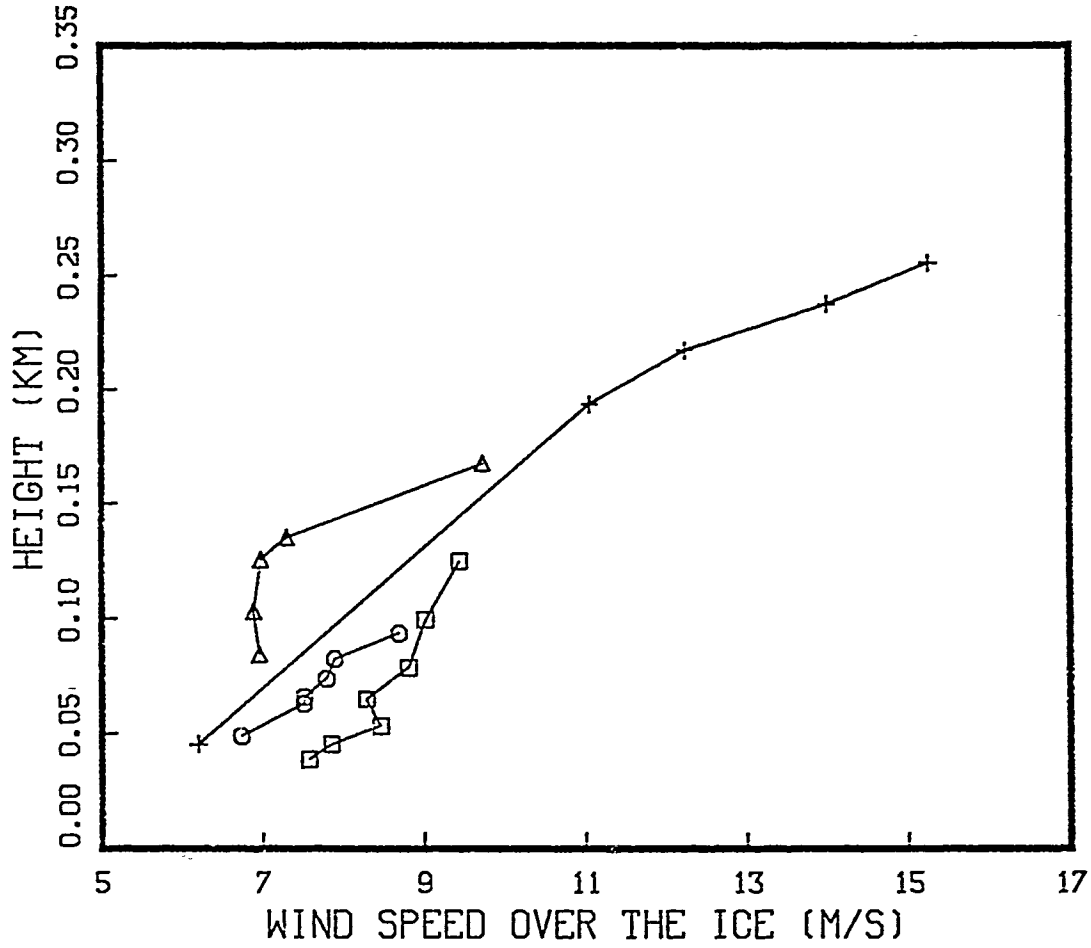

Figure 7. Profiles of wind speed over ice

oceanward of the ice edge. The cloud base was at approximately 225 m. In the vicinity of showers, the cloud base was lower. The stratocumulus layer gradually thinned to no clouds over the ice. The lidar-derived cloud layer base was compared to the calculated lifting condensation level (LCL). The dashed line on Figure 8 identifies the LCL. The results were generally consistent, though the LCL was approximately 25 m lower. The cloud top was used as an estimate of the boundary layer height (h). This method could not be used to determine h over the ice, since there were no clouds. The potential temperature profiles were well-mixed in the ABL and virtually identical above the ABL over

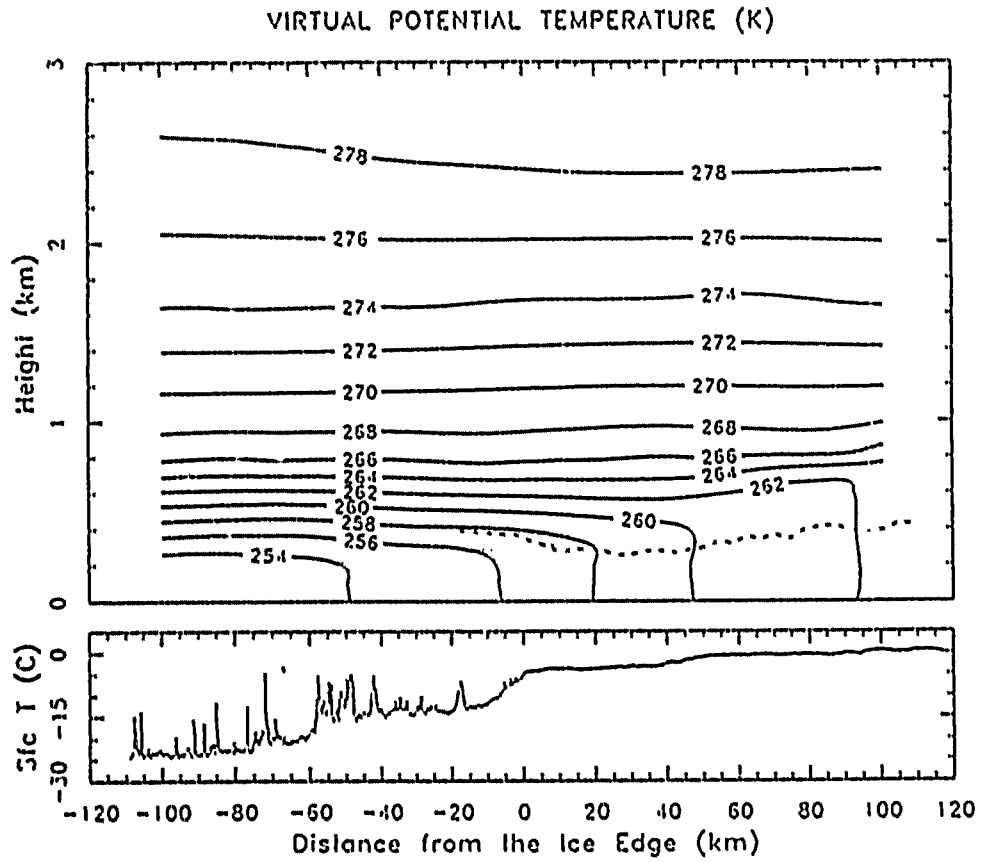

Figure 8. Cross section of virtual potential temperature: Flight path was perpendicular to the ice edge (x = 0). Ice is to the left of x = 0 and ocean to the right. The shaded area is the stratocumulus deck as detected by lidar. The dashed line over the water is the lifting condensation level, determined from 45 meter data. The dotted line over the ice is the estimated boundary layer height, also determined from 45 meter data.

Source: Shaw et al., (1990)

the ice and ocean. The boundary layer height (h) was estimated by assuming that the 45 m leg potential temperature data represented the ABL well-mixed value. Then the height where this same potential temperature value was found on the free-atmosphere profile was considered the ABL depth. This method assumes a barotropic atmosphere above the inversion in the cross-ice edge direction and therefore does not allow for a thermal wind component parallel to the ice edge. This assumption is not quite correct, since the influence of subsidence from the large scale inverted ridge would act to increase the temperature gradient in the sloping inversion and make a thermal wind component parallel to the ice edge likely. However, the parameterization appeared to give a reasonable estimate of h over the ice. The lidar cloud top height observations were in close agreement with the parameterized h values near the ice edge.

The specific humidity traces (Figure 9) showed that within the ABL, the air over the ocean was twice as moist (1.2 g kg^{-1}) as the air over the ice (.6 g kg^{-1}). The atmosphere above the ABL was quite dry with specific humidity values of .4 g kg^{-1} just above the ABL and .2 g kg^{-1} at approximately 1400 m. In agreement with the thermal structure, the strongest horizontal moisture gradient was in the region 40 km oceanward of the ice edge.

Windspeed (Figure 10) varied by only 1 m s^{-1} along the 200 km flight legs above the ABL. Within the boundary layer over the ocean, the windspeed was within 1 m s^{-1} of the windspeed above the ABL. Over the ice, however, the windspeed near the surface varied from 11 m s^{-1} at the ice edge to about 6 m s^{-1} at 100 kilometers from the ice edge. The strongest horizontal windspeed variation occured in the region more than 40 km iceward of the ice edge.

The wind direction cross-section (Figure 11) showed a variation of approximately 10° at most, on all horizontal flight legs. The near surface wind was from approximately 25°. Between the surface and 900 mb (about 800 m), the wind veered no more than 10

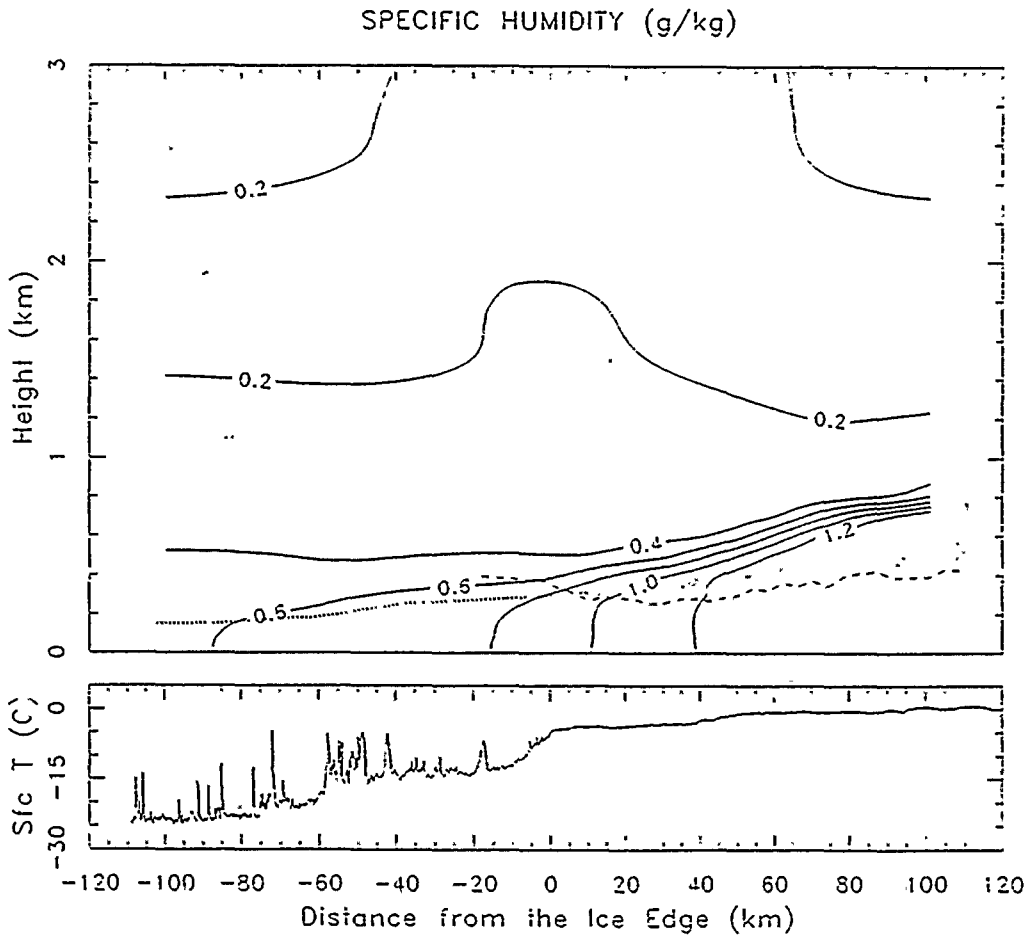

Figure 9. Cross section of specific humidity: Flight path was perpendicular to the ice edge. The shaded area is the stratocumulus deck as detected by lidar. The dashed line over the water is the lifting condensation level, determined from 45 meter data. The dotted line over the ice is the estimated boundary layer height, also determined from 45 meter data.

Source: Shaw et al., (1990)

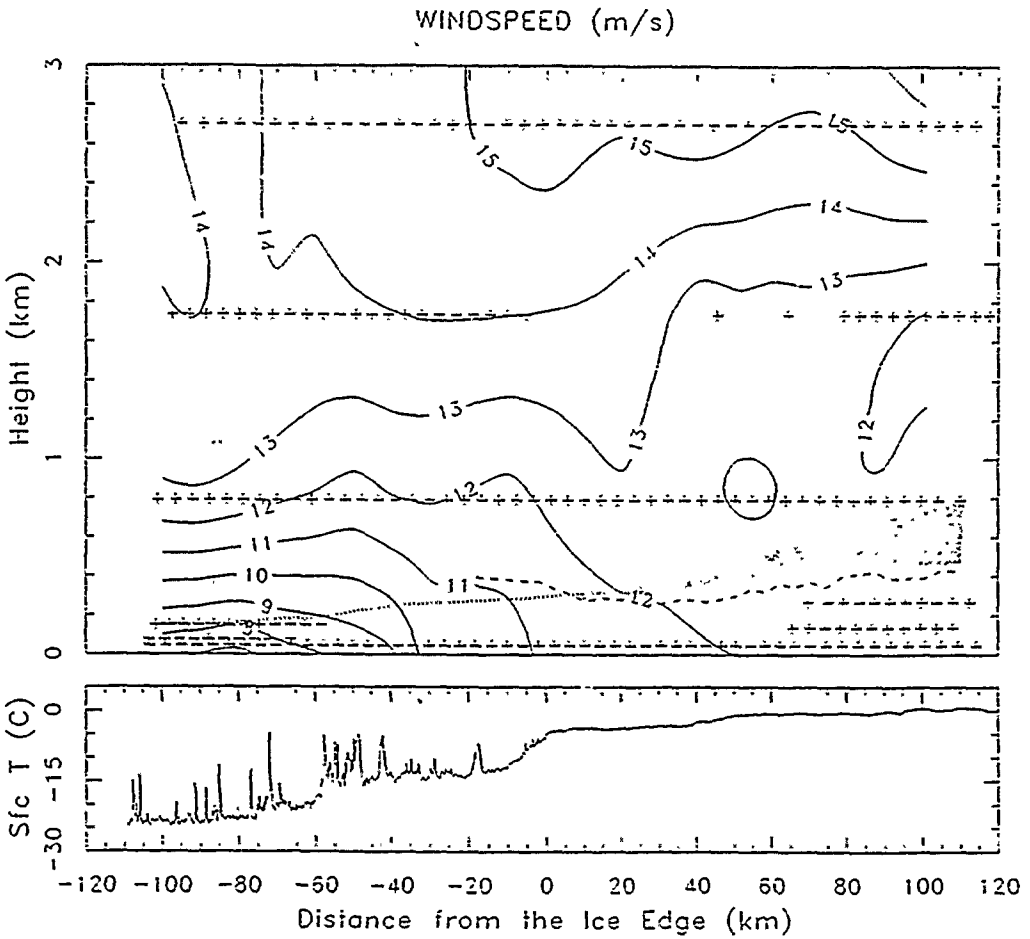

Figure 10. Cross section of wind speed, perpendicular to the ice edge.
Source: Shaw et al., (1990)

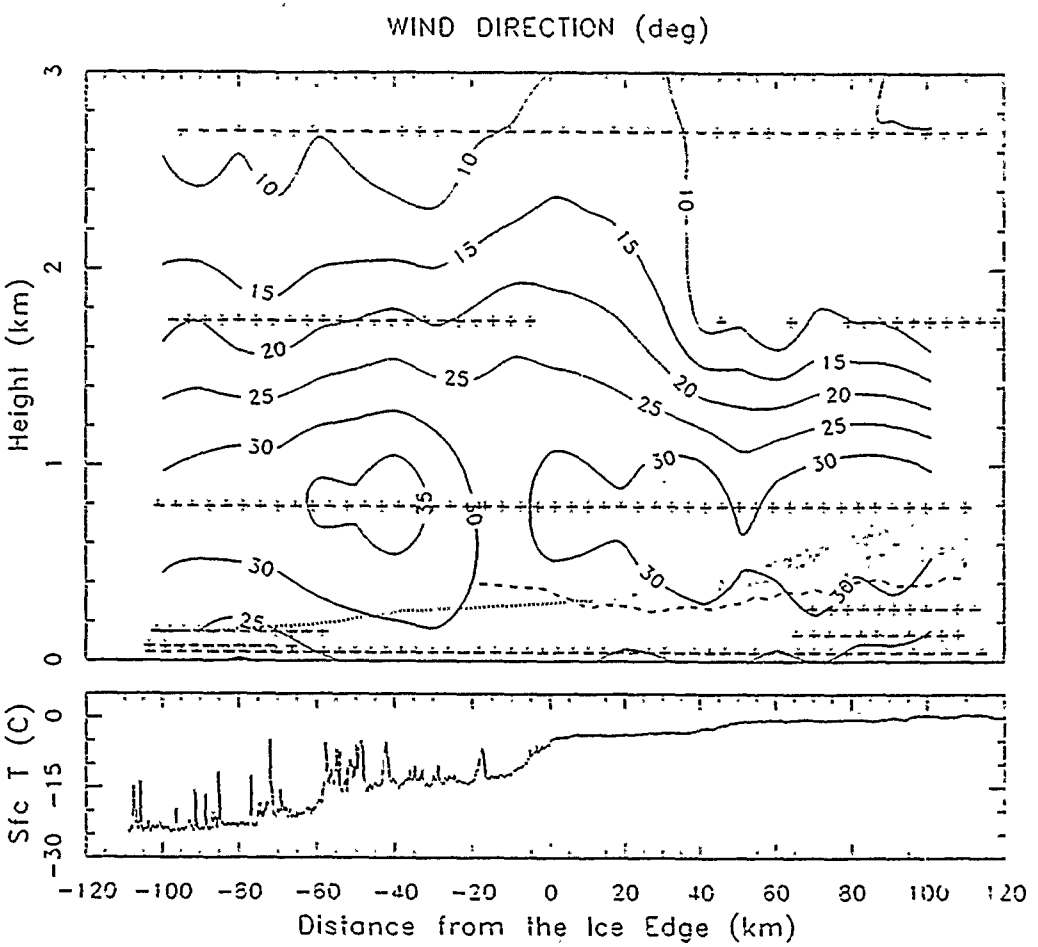

Figure 11. Cross section of wind direction, perpendicular to the ice edge.
Source: Shaw et al., (1990)

to 12° . Between altitudes of 1 and 3 km, the wind backed 20° . This implies cold advection. However, some of the variation may be due to unaccounted for drifts in the INS system. Therefore, the wind direction changes, particularily above the ABL where the changes are small, should be regarded with some caution.

C. HORIZONTAL GRADIENTS

The flight pattern with its parallel and perpendicular ice edge legs allowed horizontal gradients to be determined at two levels over both the ice and ocean. Figure 12 shows the spatial series for u, v and virtual temperature and their linear best fit from the 50 km segment at the end of the 45 m flight leg over the ocean. u and v are in ice edge coordinates with positive u towards the ocean. A linear best fit was obtained for each variable. This provided a measure of how much a variable changed (its delta value) along the flight leg. The delta values were used to determine the components of the horizontal gradient using a least squares method for heights of 40 and 150 m over the ice and 45 and 267 m over the ocean. Results are listed in Table 2. Using temperature T as an example, values of ΔT, Δx, and Δy derived from each leg were used in:

$$\Delta T \simeq \frac{\partial T}{\partial x}\Delta x + \frac{\partial T}{\partial y}\Delta y$$

This is of the form z = ax + by. The least squares method minimizes $\sum_i (z - z_i)^2$ with respect to a and b.

$$\frac{\partial}{\partial a}\sum_i [z_i - (ax_i + by_i)]^2 = 0$$

and

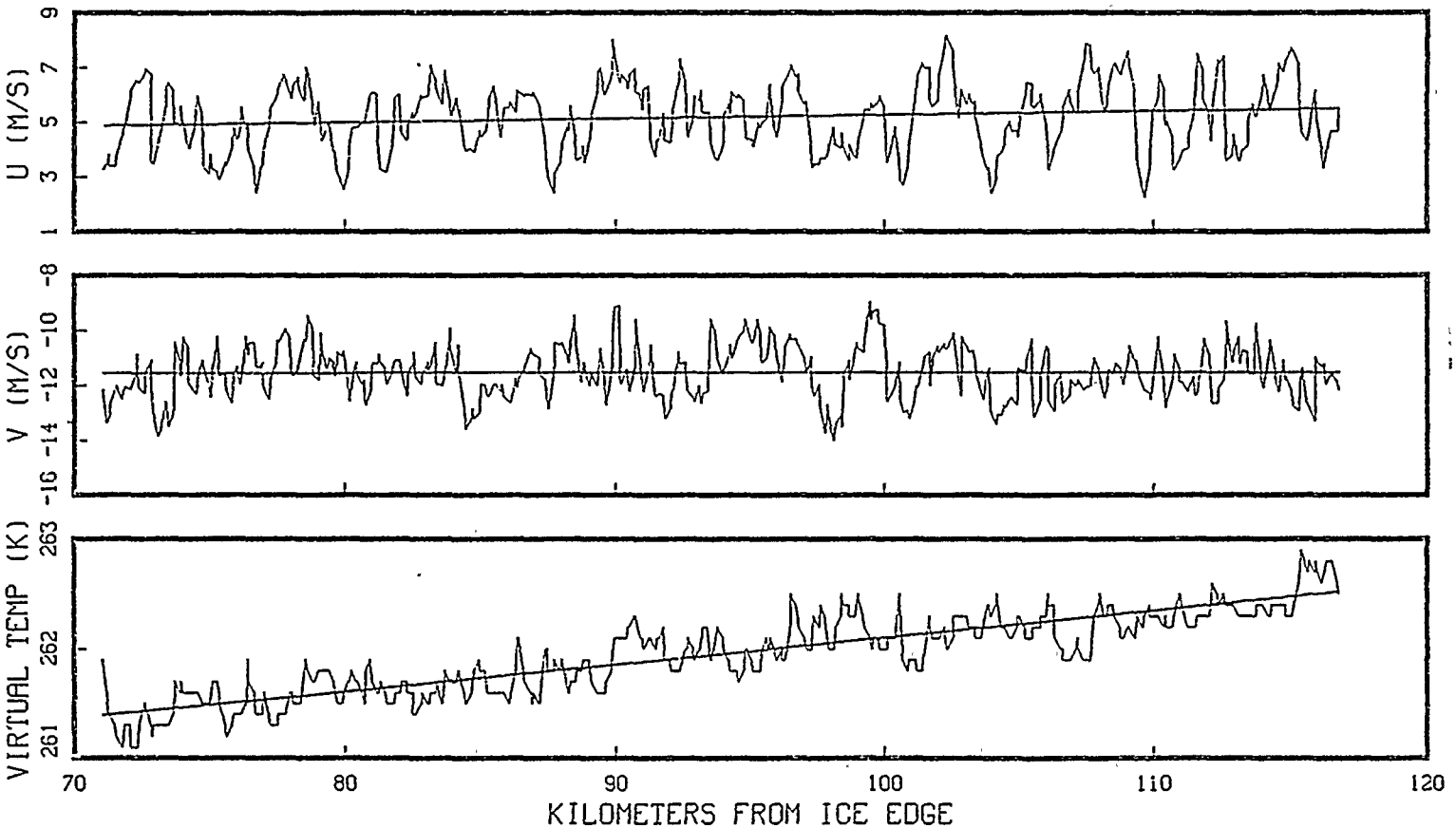

Figure 12. u, v and virtual temperature spatial series: from the 45 meter flight leg over ocean.

$$\frac{\partial}{\partial b}\sum_i [z_i - (ax_i + by_i)]^2 = 0$$

Expanding and rearranging gives:

$$a = \frac{\sum_i y_i^2 \sum_i x_i z_i - \sum_i y_i z_i \sum_i x_i y_i}{\sum_i x_i^2 \sum_i y_i^2 - \left(\sum_i x_i y_i\right)^2}$$

and

$$b = \frac{\sum_i x_i^2 \sum_i y_i z_i - \sum_i x_i z_i \sum_i x_i y_i}{\sum_i x_i^2 \sum_i y_i^2 - \left(\sum_i x_i y_i\right)^2}$$

The gradient calculation for pressure was slightly different. Figure 13 shows the pressure series reflected the variation of the aircraft's altitude. Using the radar altimeter height (z) values and the hydrostatic approximation, the pressure was adjusted to a constant flight altitude (z_{ref}) then used in the gradient calculation.

$$\frac{\partial p}{\partial z} = -\rho g$$

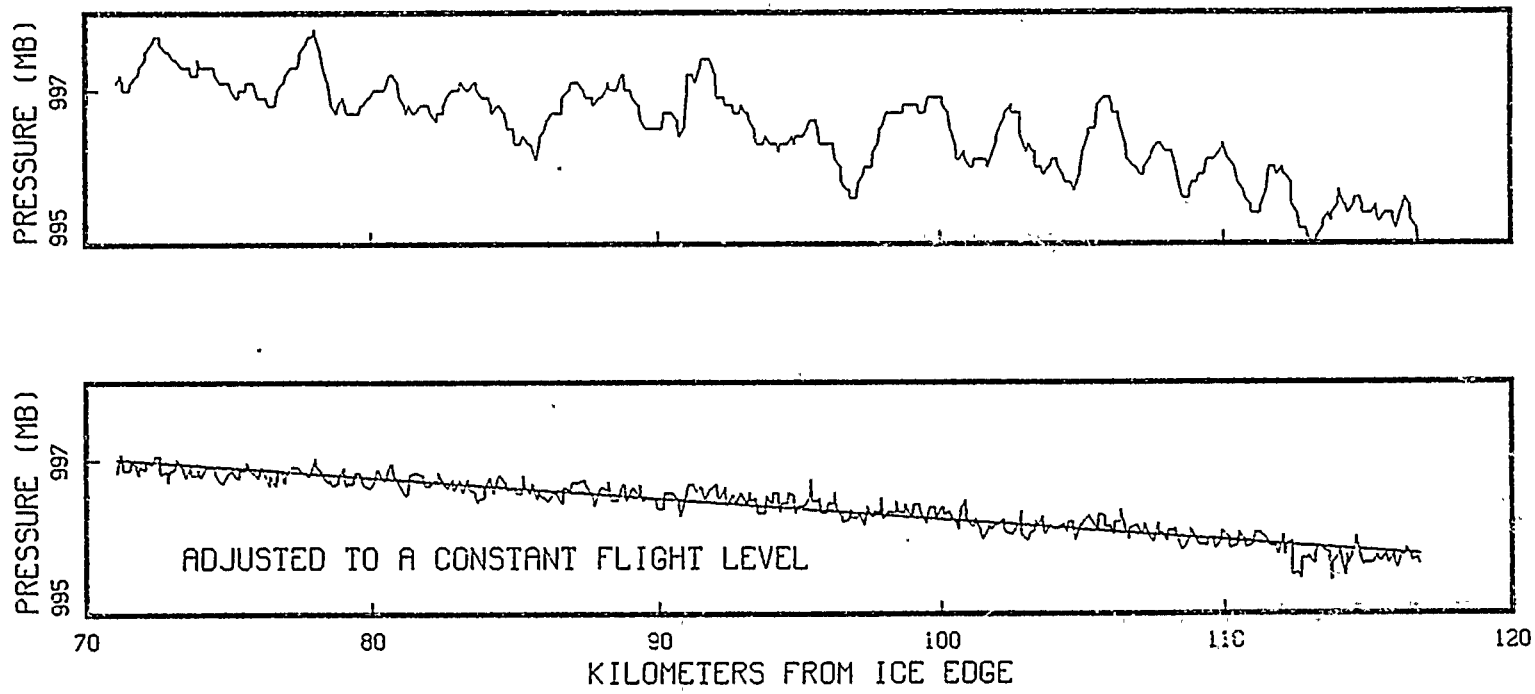

Figure 13. Pressure spatial series: from the 45 meter flight leg over ocean.

$$p = \rho R T_V$$

$$\rho = \frac{p}{R T_V}$$

where p is pressure, ρ is density, g is gravity, R is the specific gas constant, and T_V is virtual temperature which is assumed constant over small altitude changes. Substituting this into the hydrostatic approximation and integrating gives:

$$\ln\left(\frac{p}{p_{ref}}\right) = -\frac{g}{R T_V}(z - z_{ref})$$

$$\frac{p}{p_{ref}} = \exp\left[-\frac{g}{R T_V}(z - z_{ref})\right]$$

$$p_{ref} = p \exp\left[\frac{g}{R T_V}(z - z_{ref})\right]$$

where p_{ref} is the pressure adjusted to a constant flight altitude.

Figure 14 is the specific humidity series from the dewpointer and the microwave refractometer (10 s averages). The mean has been subtracted from the refractometer data. This is why the mean values differ between the two series. The dewpointer's tendency to overshoot a step change affected the delta values. For this reason, the microwave refractometer data were used to calculate the horizontal specific humidity gradients. Table 2 summarizes the horizontal gradients over the ice and ocean. The gradients are with respect to the ice edge coordinate system where positive x is towards the ocean and positive y is along the ice edge towards the northeast. The geostrophic wind was calculated using the pressure gradient. The other gradients were used in determining the physical balances described in the next chapter.

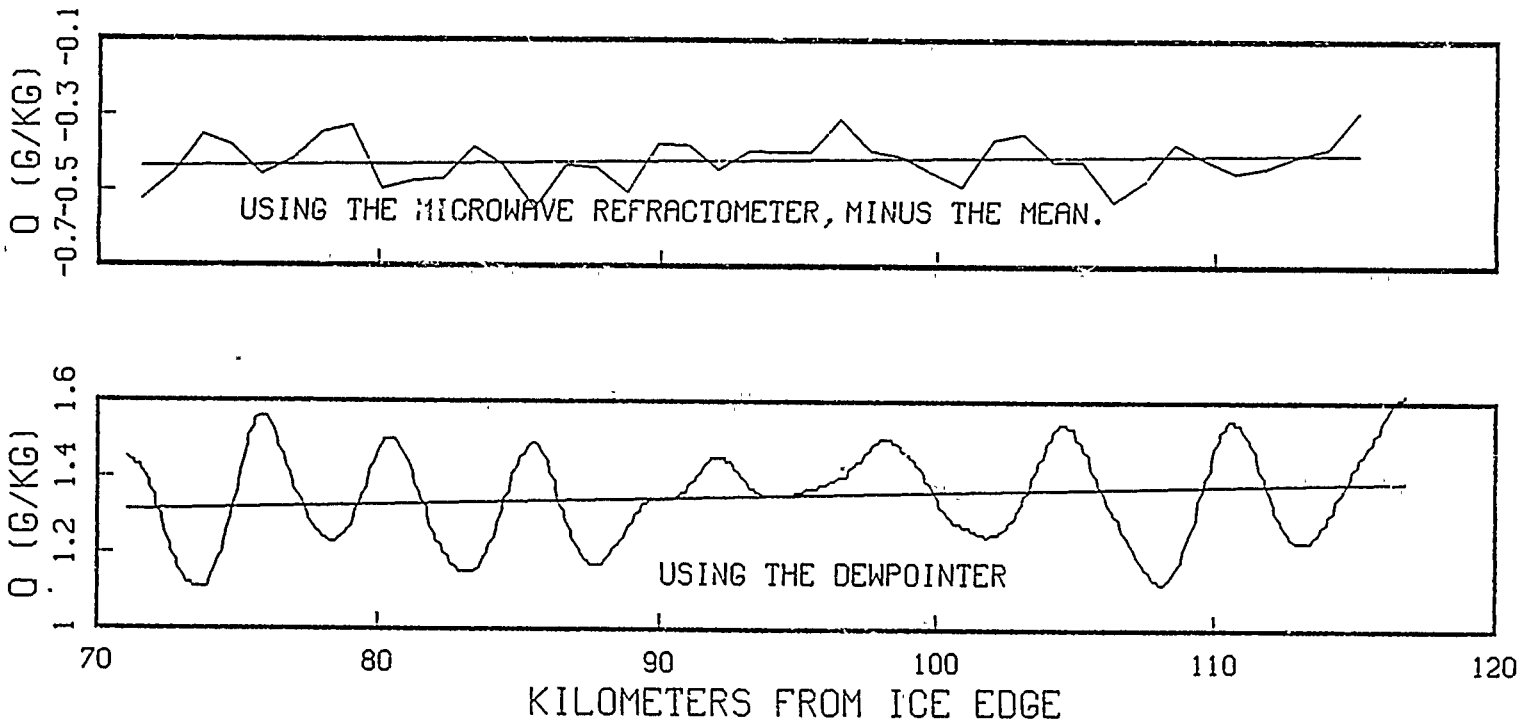

Figure 14. Specific humidity spatial series: from the 45 meter flight leg over ocean.

Table 2. GRADIENTS DERIVED USING THE LEAST SQUARES METHOD

	Over ice		Over ocean	
	40 m	150 m	45 m	267 m
$\frac{\partial p}{\partial x}$ (mb / km)	-.00905	-.02287	-.02215	-.01498
$\frac{\partial p}{\partial y}$ (mb / km)	.00364	.00036	-.00194	-.00262
$\frac{\partial T}{\partial x}$ (K / km)	.02010	.01547	.02555	.03319
$\frac{\partial T}{\partial y}$ (K / km)	-.00847	-.00522	-.02460	-.02947
$\frac{\partial q}{\partial x}$ (g / kg km)	.00309	.00261	.00089	.00322
$\frac{\partial q}{\partial y}$ (g / kg km)	-.00457	.00211	-.00097	-.00616
$\frac{\partial u}{\partial x}$ (m / s km)	.04815	-.0123	.00604	.02118
$\frac{\partial u}{\partial y}$ (m / s km)	.00213	.01334	.02745	.03648
$\frac{\partial v}{\partial x}$ (m / s km)	-.00143	-.00442	-.00159	.00526
$\frac{\partial v}{\partial y}$ (m / s km)	.02088	.00745	.01097	.01119

D. GEOSTROPHIC WIND

The geostrophic wind ($\vec{V}_g$) was calculated using the gradients from the pressure sensor data.

$$u_g = -\frac{1}{f\rho}\frac{\partial p}{\partial y}$$

$$v_g = \frac{1}{f\rho}\frac{\partial p}{\partial x}$$

Figure 15 shows the geostrophic wind over the ice and ocean. $\vec{V}_g$ at 40, 45, 150 and 267 m was calculated using the pressure gradients. Since 900 mb was at all times above the ABL, the actual wind at that level is considered geostrophic. Over the ocean, the geostrophic wind decreased in magnitude between 45 and 267 m. This is consistent with the ABL thermal gradients. The thermal wind ($\vec{V}_t$) defined by the geostrophic wind change with height, blows with low temperature to the left. Over the ice, the geostrophic wind changes in magnitude and direction between 40 and 150 m. This is not consistent with the ABL thermal gradients since $\vec{V}_t$ defined by the change of $\vec{V}_g$ with height does not blow with low temperature to the left. It is the inversion temperature gradient noted in Figure 4 that accounts for the $\vec{V}_g$ change. Above the ABL, $\vec{V}_g$ over the ice and ocean has comparable magnitude and direction. Thus, over the ice, $\vec{V}_g$ is relatively constant with height within the ABL but changes significantly in the inversion, while over the ocean, $\vec{V}_g$ changes significantly in the ABL. This relation has implications concerning the momentum balance described in the next chapter.

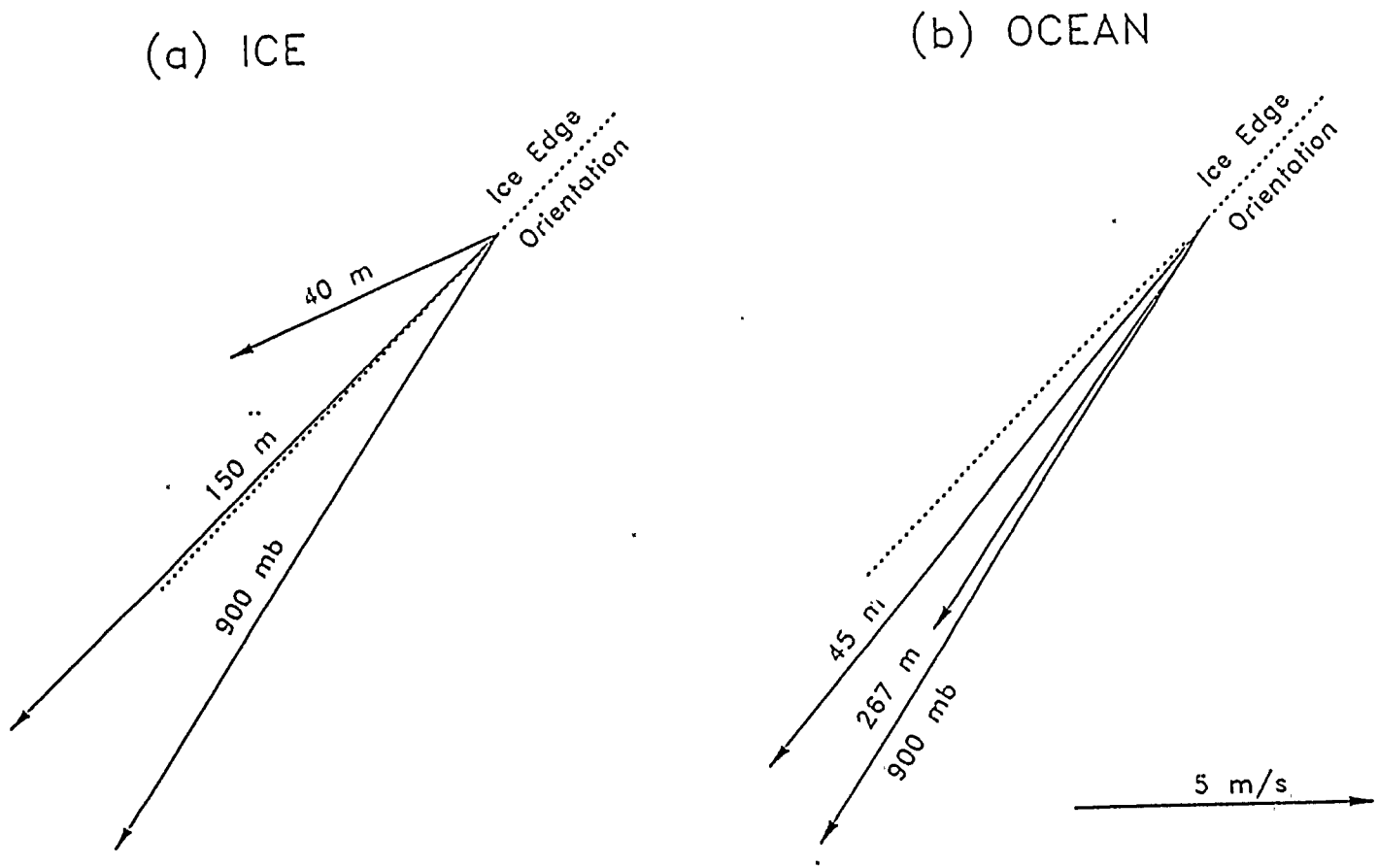

Figure 15. Geostrophic wind
Source: Shaw et al., (1990)

IV. TURBULENCE MEASUREMENTS

This section describes the heat, moisture and momentum balances in the ABL applied at the corners of the flight pattern over the ice and ocean. An ice edge coordinate system is used with positive x towards the ocean and positive y along the ice edge towards the northeast.

A. HEAT BALANCE

The time rate of change of potential temperature, neglecting radiation, is:

$$\frac{\partial \theta}{\partial t} = -u\frac{\partial \theta}{\partial x} - v\frac{\partial \theta}{\partial y} - \frac{\partial \overline{w'\theta'}}{\partial z}$$

where θ, u and v are the mean potential temperature and velocity, and w' and θ' are the turbulent vertical velocity and potential temperature. The coordinate system is such that x is perpendicular to the ice edge and positive toward the ocean. The advection terms represent cross-ice ($u\frac{\partial \theta}{\partial x}$) and along-ice advection ($v\frac{\partial \theta}{\partial y}$). The time rate of change of potential temperature was determined from two flight legs, along the same course but at different altitudes, which were separated by approximately 1 hr. This is appropriate since both flight legs were in the ABL, and the potential temperature profile was well mixed. The velocity components, u and v, were determined from 20 km segments at the flight pattern corners. The average vertical turbulent heat flux ($\overline{w'\theta'}$) was determined (see Chapter II, sections B and C) for the 40 km segments closest to the flight pattern corners. Figure 16 shows the $\overline{w'\theta'}$ profiles and linear best fit which was forced to zero at .8h where h is the height of the ABL (120 m over ice, 600 m over ocean). The best fit was forced to zero at .8h since this is the expected height where the heat flux changes sign due to entrainment of higher temperature air from above the inversion base.

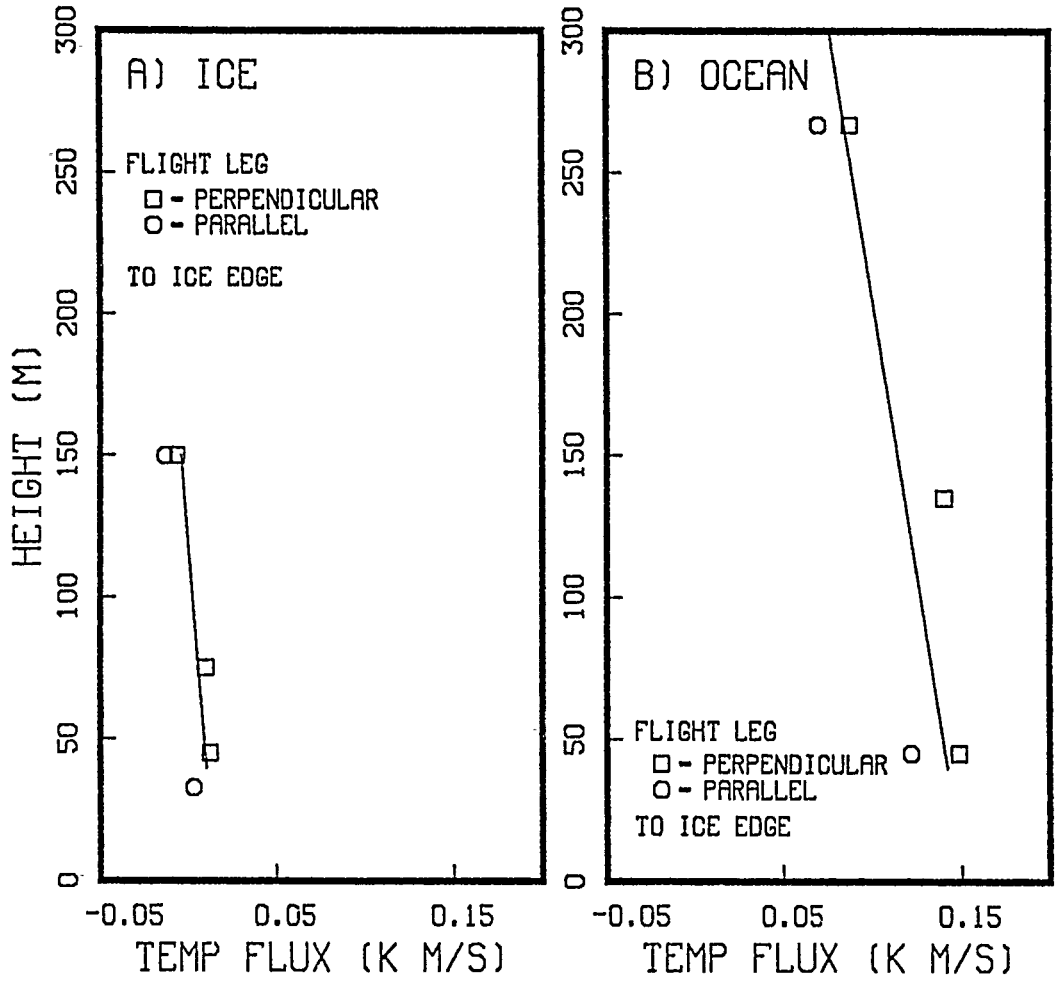

Figure 16. Vertical turbulent heat flux

Table 3 shows the heat balance over the ice and ocean. Over the ice, there was no detectable change in potential temperature with time, while over the ocean, there was net cooling. Advection mostly balanced the vertical heat flux. Along-ice-edge advection was approximately twice as large as cross-ice advection. The magnitude of the terms was larger over the ocean than ice. Compared to the other terms, the residual was small. This strongly suggests that neglected effects did not play a large role in the balance.

Table 3. HEAT BALANCE

	$\frac{\partial\theta}{\partial t}$ (K / hr)	$-u\frac{\partial\theta}{\partial x}$ (K / hr)	$-v\frac{\partial\theta}{\partial y}$ (K / hr)	$-\frac{\partial\overline{w'\theta'}}{\partial z}$ (K / hr)	residual (K / hr)
Ice	0.00	-0.12	-0.24	0.46	0.10
Water	-0.46	-0.48	-1.15	0.91	0.26

Source: Shaw et al., (1990)

B. MOISTURE BALANCE

The time rate of change of moisture is:

$$\frac{\partial q}{\partial t} = -u\frac{\partial q}{\partial x} - v\frac{\partial q}{\partial y} - \frac{\partial\overline{w'q'}}{\partial z}$$

where q is the mean specific humidity, and q' is the fluctuating part. The time rate of change, u, v and the average vertical moisture flux ($\overline{w'q'}$) were obtained by the same method used with the heat balance. Figure 17 shows the $\overline{w'q'}$ profiles and linear best fit which was forced to zero at h (150 m over ice, 750 m over ocean). The best fit was forced to zero at h since upward moisture flux is expected to decrease with height up to the inversion base.

Table 4 shows the moisture balance over ice and ocean. The time rate of change reflects net drying of the ABL. Over the ocean, advection partially balances the vertical moisture flux. The magnitude of the residual indicates this description of the moisture balance was not as successful as with the heat balance. The Figure 17 best fit over the ocean does not reflect the observed increase of the moisture flux with height over the lower ABL. This increase with height indicates drying near the surface and moistening of higher levels. This suggests there is a moisture source in the ABL other than the flux

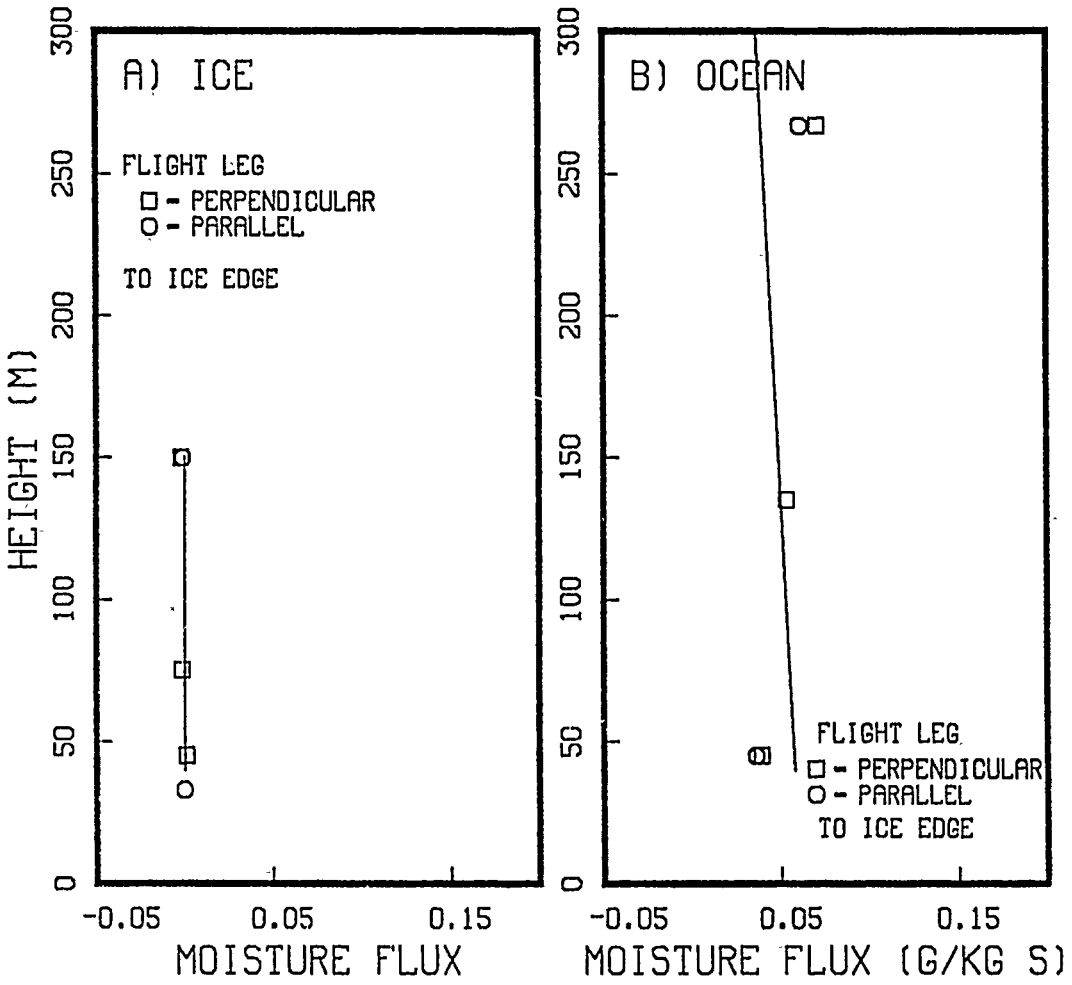

Figure 17. Vertical turbulent moisture flux

from the ocean surface. A similar increase of $\overline{w'q'}$ with height over the ocean was noted in a study by Nicholls and Readings (1979). Their observations showed $\overline{w'q'}$ increased with height over the lower ABL and decreased with height in the upper ABL. The mean specific humidity decreased with height throughout the mixed layer. They concluded the increasing $\overline{w'q'}$ profile was acting to change the decreasing mean profile to a mor well mixed (constant) profile. The situation during the CEAREX flight differed slightly in that the mean specific humidity profile didn't decrease with height throughout the mixed

layer. However, Figure 4 shows it was not so well mixed at the lower levels. No observations were available to determine if $\overline{w'q'}$ decreased with height in the upper ABL.

The moisture flux increase with height implies a downward transfer of water vapor in the boundary layer. For this to occur, a moisture source above the surface is required. Donelan and Miyake (1973) suggested evaporation of water droplets released from the surface by whitecapping as a possible moisture source that could explain the flux increase with height.

Table 4. MOISTURE BALANCE

	$\frac{\partial q}{\partial t}$ (g / kg hr)	$-u\frac{\partial q}{\partial x}$ (g / kg hr)	$-v\frac{\partial q}{\partial y}$ (g / kg hr)	$-\frac{\partial \overline{w'q'}}{\partial z}$ (g / kg hr)	residual (g / kg hr)
Ice	-.001709	-.00612	-.001235	-.00788	.01353
Water	-.0564	-.0137	-.14799	.29124	-.18595

C. MOMENTUM BALANCE

The momentum balance, neglecting accelerations is:

$$\frac{\partial \overline{u'w'}}{\partial z} = f(v - v_g) \tag{1}$$

$$-\frac{\partial \overline{v'w'}}{\partial z} = f(u - u_g) \tag{2}$$

The above equations say that the difference between the pressure gradient force (fv_g) and the coriolis force (fv) is balanced by the momentum flux divergence (stress). Therefore, the difference between the observed and geostrophic wind is related to the stress profiles. If the difference is constant, the stress changes linearly with height. If the difference isn't constant, curvature in the stress profile results. The observed wind averages for the flight levels within the ABL are listed in Table 5.

Table 5. OBSERVED WIND AVERAGES

height	u (m/s)	v (m/s)
Ice 75m	3.05	-6.78
Ice 40m	1.47	-6.75
Ocean 267m	3.65	-12.22
Ocean 135m	3.75	-11.67
Ocean 45m	4.8	-11.95

1. Over the Ice

Table 5 indicates that u varies and v is constant with height over the ice. Recall that over the ice, $\vec{V}_g$ did not vary with height within the ABL since the boundary layer was too shallow for the thermal wind to have a significant effect. So, when applying the momentum balance in the ABL, $\vec{V}_g$ is assumed to be constant with height. Since v_g and v are considered constant, their difference is constant and equation (1) requires the profile of $\overline{u'w'}$ to be linear. Figure 18 shows the $\overline{u'w'}$ profile and linear best fit. The coordinate system is oriented such that the $\overline{u'w'}$ profile is perpendicular to the ice edge.

The u wind component varies in the boundary layer. Assuming that u varies linearly with height allows u to be described by:

$$u = u_o + \frac{\Delta u}{\Delta z} z \tag{3}$$

where u_o is u at the surface and z is the height above the surface. Integrating equation (2) over height gives:

$$\overline{v'w'}(z) - \overline{v'w'}(0) = \int_0^z f(u_g - u)dz \tag{4}$$

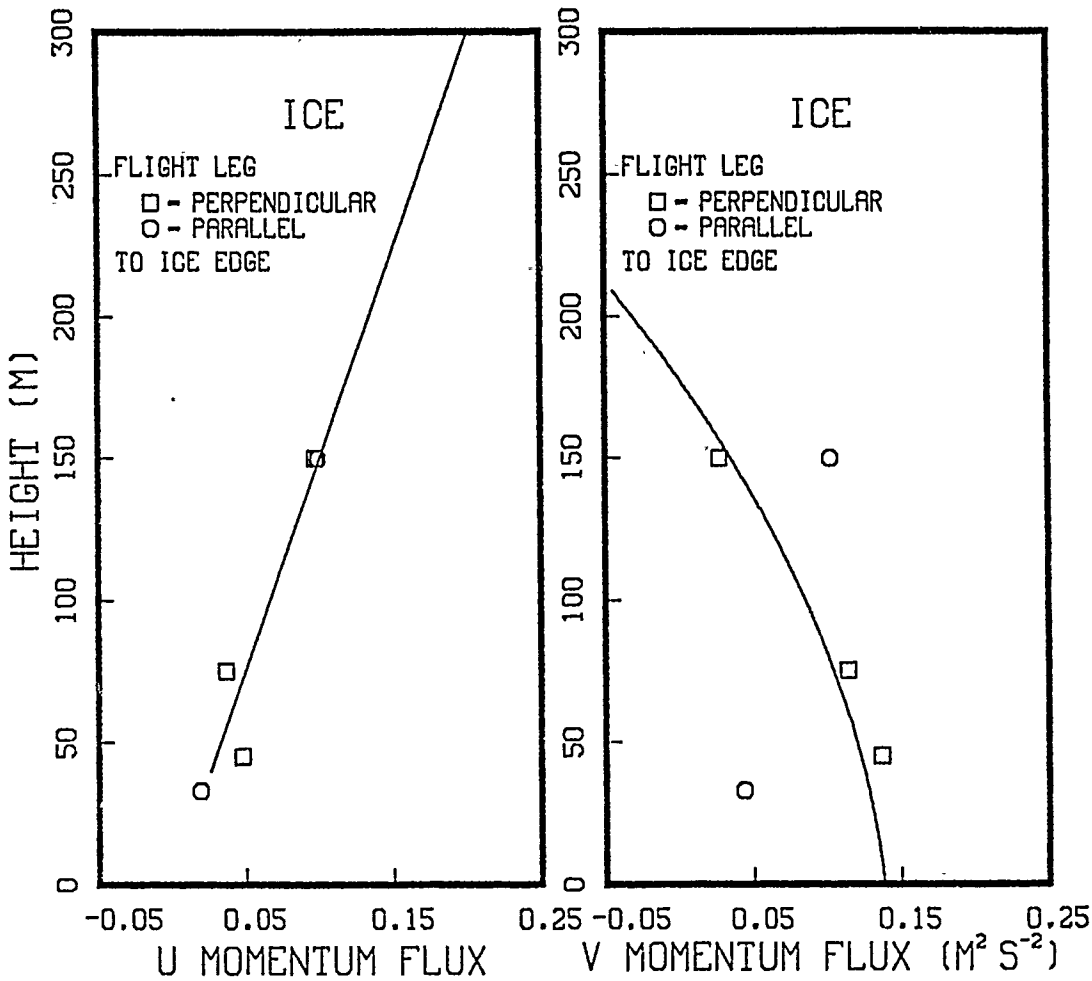

Figure 18. Vertical turbulent momentum flux over the ice

Substituting equation (3) in equation (4):

$$\overline{v'w'}(z) - \overline{v'w'}(0) = \int_0^z f\left[u_g - u(0) - \frac{\Delta u}{\Delta z} z\right] dz \tag{5}$$

Integrating and rearranging yields:

$$\overline{v'w'}(z) = \overline{v'w'}(0) + fz\left[u_g - u(0) - \frac{1}{2}\frac{\Delta u}{\Delta z} z\right] \tag{6}$$

Equation (6) describes the best fit curve. Using the $\overline{v'w'}$ averages from the various altitudes, a least squares method was used with this curve to obtain $\overline{v'w'}(0)$. Table 5 values were used for $\frac{\Delta u}{\Delta z}$, and equation (3) was solved for u(0). Figure 18 shows the $\overline{v'w'}$ profile and best fit defined by equation (6). The coordinate system is oriented such that the $\overline{v'w'}$ profile is parallel to the ice edge. The curve closely matches the observed $\overline{v'w'}$ averages of the flight legs perpendicular to the ice edge while there's some scatter for the flight legs parallel to the ice edge. The closeness of the best fits to the observed values confirms that the neglected inertia terms did not have a dominant role.

2. Over the Ocean

The large heat flux and surface stress produced a strong mixed layer with little change of observed winds with height (Table 5). Recall that over the ocean, the magnitude of $\vec{V}_g$ varied with height in the ABL (Figure 15) due to the temperature gradient. Table 6 lists the geostrophic wind components over the ocean.

Table 6. GEOSTROPHIC WIND AVERAGES

height	u_g (m/s)	v_g (m/s)
Ocean 267m	1.44	-8.21
Ocean 45m	1.04	-11.90

Table 6 indicates that u_g is relatively constant and v_g varies with height. Since u_g and u are considered constant, their difference is constant and equation (2) requires the profile of $\overline{v'w'}$ to be linear. Figure 19 shows the $\overline{v'w'}$ profile and linear best fit.

Assuming that v_g varies linearly with height allows v_g to be described by:

$$v_g = v_{go} + \frac{\Delta v_g}{\Delta z} z \tag{7}$$

where v_{go} is v_g at the surface. Integrating equation (1) over height gives:

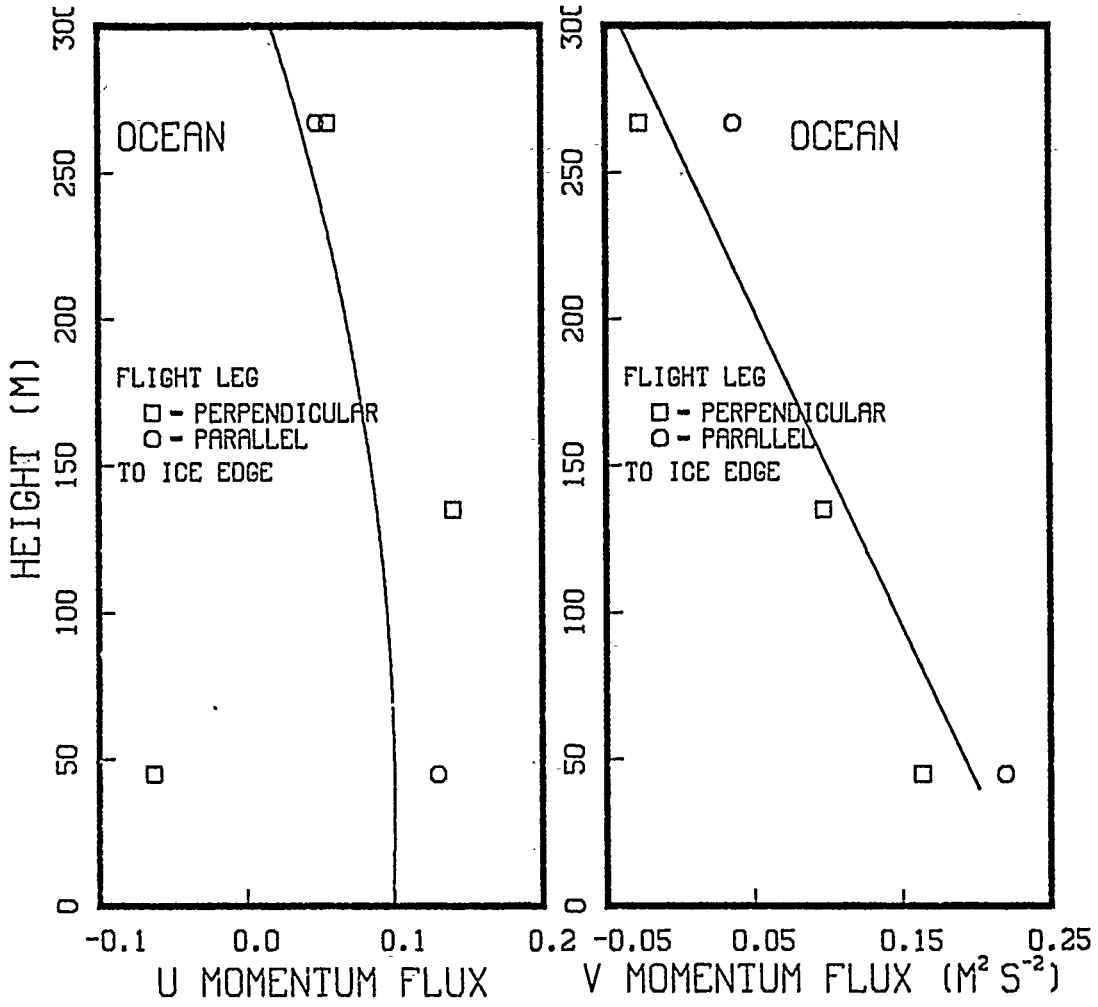

Figure 19. Vertical turbulent momentum flux over the ocean

$$\overline{u'w'}(z) - \overline{u'w'}(0) = \int_0^z f(v - v_g)dz \tag{8}$$

Substituting equation (7) in equation (8):

$$\overline{u'w'}(z) - \overline{u'w'}(0) = \int_0^z f\left[v - v_g(0) - \frac{\Delta v_g}{\Delta z} z\right]dz \tag{9}$$

$$\overline{u'w'}(z) = \overline{u'w'}(0) + fz\left[v - v_g(0) - \frac{1}{2}\frac{\Delta v_g}{\Delta z} z \right] \tag{10}$$

Equation (10) describes the expected functional form of the variation of $\overline{u'w'}$ with height. Table 6 values were used for $\frac{\Delta v_g}{\Delta z}$, and equation (7) was solved for $v_g(0)$. Using the $\overline{u'w'}$ averages from the various altitudes, a least squares method was used with this curve to obtain $\overline{u'w'}(0)$. Then $\overline{u'w'}(0)$ was used in equation (10) to obtain the best fit. Figure 19 shows the $\overline{u'w'}$ profile and best fit. The negative $\overline{u'w'}$ of the 45 m flight leg remains unexplained. There were no indications of equipment malfunction.

V. SUMMARY

Data collected with the NOAA P-3 research aircraft was used to examine the mean structure and physical balances of the ABL in the MIZ. The wind flow was nearly parallel to the ice edge with the 900 mb geostrophic wind approximately 15° off-ice. The atmospheric conditions above the ABL, were virtually identical at 100 km from the ice edge over both the ice and ocean. Therefore, the structure of the ABL was due to interaction with the surface. The well mixed boundary layer extended at least 100 km into the ice. The horizontal gradients of temperature and moisture were maximum at approximately 40 km oceanward of the ice edge but no boundary layer front was evident.

The heat balance showed that the vertical heat flux was mostly balanced by advection. Over the ocean, the magnitude of both the heat flux and advection was quite large. The residuals were small compared to the other terms. This strongly suggests that neglected effects did not play a major role.

The moisture balance gave an unusual result. Over the ocean, the profile of vertical moisture flux increased with height over the lower ABL. This profile could be viewed as acting to make the mean specific humidity profile more constant or it could be describing the presence of a counter-gradient flux.

The relationship between the observed and geostrophic winds in the momentum balance explained the curvature in the stress profiles. The boundary layer was sufficiently deep over the ocean, to allow the horizontal temperature gradient to affect the geostrophic wind. Over the ice the ABL was shallow, thus minimizing this effect.

These observations provide evidence of the interactions occuring in the MIZ under conditions of flow nearly parallel to the ice edge. The sloping inversion and horizontal temperature gradient had a significant effect on the geostrophic wind in the ABL. The

geostrophic forcing in turn affected the surface stress. The magnitude and variability of these interactions are important for understanding ice, ocean and atmospheric dynamics in the MIZ.

REFERENCES

Bennett T.J., and K. Hunkins, 1986: Atmospheric boundary layer modification in the marginal ice zone. *J. Geophys. Res.*, 91, 13033-13044.

Davidson, K.L., and P.S. Guest, 1987: NPS meteorology studies on the marginal ice zone. *Naval Res. Rev.*, 1, 28-35.

Donelan, M., and M. Miyake, 1973: Spectra and fluxes in the boundary layer of the trade-wind zone. *J. Atmos. Sci.*, 30, 444-464.

Fairall, C.W., and R. Markson, 1987: Mesoscale variations in surface stress, heat fluxes, and drag coefficient in the marginal ice zone during the 1983 marginal ice zone experiment. *J. Geophys. Res.*, 92, 6921-6932.

Greenhut, G.K., and R.O. Gilmer, 1985: Calibration and accuracy of the NOAA/ERL gust probe system and intercomparison with other systems. NOAA Tech. Memo. ERL ESG-22, Boulder, CO, 30 pp.

Holland, J.Z., 1968: *An Application of Some Statistical Techniques to the Study of Eddy Structures.* Ph.D. dissertation, University of Washington, Seattle, WA, 378 pp.

Johannessen, O.M., 1987: Introduction: Summer marginal ice zone experiments during 1983 and 1984 in Fram Strait and the Greenland Sea. *J. Geophys. Res.*, 92, 6716-6718.

Johannessen, O.M., J.A. Johannessen, J. Morison, B.A. Farrelly, and E.A.S. Svendsen, 1983: Oceanographic conditions in the marginal ice zone north of Svalbard in early fall 1979 with an emphasis on mesoscale processes. *J. Geophys. Res.*, 88, 2755-2769.

Kantha, L.H., and G.L. Mellor, 1989: A numerical model of the atmospheric boundary layer over a marginal ice zone. *J. Geophys. Res.*, 94, 4959-4970.

Kellner, G., C. Wamser, and R.A. Brown, 1987: An observation of the planetary boundary layer in the marginal ice zone. *J. Geophys. Res.*, 92, 6955-6965.

Lackmann, G.M., P.S. Guest, K.L. Davidson, R.J. Lind, and J. Gonzalez, 1989: CEAREX/Polarbjoern meteorology atlas. Tech. Rpt. NPS-63-89-005, Naval Postgraduate School, Monterey, CA, 545 pp.

McPhee, M.G., 1983: Greenland Sea ice/ocean margin. *EOS*, 64, 82-83.

Nicholls, S., and C.J. Reading, 1979: Aircraft observations of the structure of the lower boundary layer over the sea. *Quart. J. Roy. Meteor. Soc.*, 105, 785-802.

Overland, J.E., R.M. Reynolds, and C.H. Pease, 1983: A model of the atmospheric boundary layer over the marginal ice zone. *J. Geophys. Res.*, 88, 2836-2840.

Reynolds, M., 1984: On the local meteorology at the marginal ice zone of the Bering Sea. *J. Geophys. Res.*, 89, 6515-6524.

Shapiro, M.A., and L.S. Fedor, 1989: A case study of an ice-edge boundary layer front and polar low development over the Norwegian and Barents Seas. In *Polar and Arctic Lows.* P.F. Twitchell, E.A. Rasmussen, and K.L. Davidson (Ed.), A. Deepak, Hampton, VA, 257-276.

Shaw, W.J., R.L. Pauley, T.M. Gobel, and L.F. Radke, 1990: A case study of the atmospheric boundary layer mean structure for flow parallel to the ice edge: aircraft observations from CEAREX. *J. Geophys. Res.*, accepted for publication.

Shaw, W.J., 1988: Inertial drift correction for aircraft-derived wind fields. *J. Atmos. and Ocean. Tech.*, 5, 774-782.

Sorbjan, Z., 1989: *Structure of the Atmospheric Boundary Layer.* Prentice Hall, Englewood Cliffs, NJ, 317 pp.

Thorndike, A.S., and R. Colony, 1982: Sea ice motion in response to geostrophic winds. *J. Geophys. Res.*, 87, 5845-5852.

Walsh, J.E., and C.M. Johnson, 1979: An analysis of Arctic Sea ice fluctuations, 1953-77. *J. Phys. Ocean.*, 9, 580-591.